In-situ charge reduction of electrospray plumes by unipolar corona ions

Jordi Grifoll[1] and Joan Rosell-Llompart[1,2]

[1] Department of Chemical Engineering, Universitat Rovira i Virgili, 43007 Tarragona, Spain.

[2] Catalan Institution for Research and Advanced Studies - ICREA, 08010 Barcelona, Spain.

Abstract

Obtaining uniformly-sized microparticles by electrospray drying poses challenges due to the high electric charge of the droplets, which often leads to Coulombic fissions, short lifetimes, and charge buildup on the collection. In this study, we have conducted numerical simulations to investigate the use of unipolar ions for achieving extensive droplet discharging in electrosprays, aiming to prevent Coulombic fissions and attain high efficiency in extracting the electrically discharged aerosol. Our mathematical model incorporates Lagrangian tracking of the droplets, their evaporation till forming a solid residue, Coulomb fission, Eulerian descriptions of ion and progeny droplet transports, and droplet discharge kinetics through ion capture. We have identified an effective system configuration comprising coaxially a capillary electrode supporting the Taylor cone, a nearby ring electrode, and an Earth-grounded plate with a central orifice emitting ions. The electrode potentials are selected to sustain the Taylor cone. Air flows coaxially with the electrospray, passing through the ring hole, and exiting the system through a circular slit in the plate. We have simulated two electrospray systems with identical droplet size distributions but different volatilities of the solvents (acetone and methanol). In these systems, the ion cloud rapidly expands from the plate orifice, driven by strong electrical self-repulsion, subsequently flooding the entire spray while traveling towards the ring. The droplets are electrostatically repelled from the ring and are encouraged by the airflow to pass through the ring hole. Most of the droplets are discharged downstream of the ring, before they undergo their first Coulomb fission. Importantly, when the ring is thin and short, it attracts the majority of excess ions. The remaining ions pass through the ring towards the Taylor cone, but are intercepted by the spray, thus preserving the cone stability. Consequently, our simulations demonstrate that the configuration with axial symmetry comprising a ring and an orifice plate between the spraying and corona tips is a robust strategy to obtain stable and efficient in-situ discharging and extraction of electrospray plumes.

1. Introduction

Electrosprays, the clouds made of electrified droplets released by Taylor cones, have significant applications. The best-known is Electrospray Ionization Mass Spectrometry (ESI-MS), where analyte ions in an electrosprayed solution are transferred to the gas phase, wherefrom they go into a mass spectrometer for identification (Fenn, 2003). Electrosprays are also used for thrust and control of small spacecraft, such as nanosatellites (Gamero-Castaño and Hruby, 2001; López Urdiales, 2004). Taylor cones are also used as high brilliance sources of metal ions in vacuo, particularly of Ga^+, used in the microsample preparation method known as Focused Ion Beam (FIB) (Benassayag et al., 1985). Besides these "low liquid flow rate" applications, electrosprays have been proposed for making materials for energy, catalysis, pharmaceutical, biomedical, and other application fields, in the form of: (i) thin films and coatings, and (ii) small particles (particularly, sub-micrometric) with extremely narrow size distributions (geometric standard deviation < 1.1) (Tang et al., 2017; Jaworek et al., 2018; Kelder et al., 2018; Castillo et al., 2018; Boda et al., 2018; Kavadiya and Biswas, 2018; Borra 2018).

The Taylor cone (TC) forms by the interplay between the surface tension force, which acts to hold the liquid together, and the interfacial electric force, which works to overcome this surface tension force (Rosell-Llompart et al., 2018). Electric force develops by the induction of net charges at the gas-liquid interface. Their pull on the liquid causes the ejection of a thin liquid jet which breaks up, releasing droplets. These droplets are nearly monosized (except for the appearance of satellite droplets). They also hold a high electrostatic charge, typically between 50 and 100% of the Rayleigh limit charge q_R (Gomez and Tang, 1991; Gomez and Tang, 1994; Chen et al., 1995; de Juan and Fernández de la Mora, 1997; Hartman et al., 2000; Grimm & Beauchamp, 2002; Larriba-Andaluz & Fernández de la Mora, 2010) compatible with electro-capillary stability (Saville, 1997; Lord Rayleigh, 1882). The high charge helps preserve the droplets' initial sizes in the spray by preventing droplet collisions. After some evaporation, however, the droplets reach a critical diameter at which they experience the instability known as Coulomb fission (CF) or Coulomb explosion, which releases charge from the droplet by ejecting one or two nanojets which release smaller "progeny" droplets.

List of Symbols

Roman Letter Symbols

B_{Mi}	Spalding number mass transfer for droplet i
B_{pro}	mechanical mobility coefficient for the progenies ($m^2\ s^{-1}\ V^{-1}\ C^{-1}$)
C_{ci}	$= 1 + \frac{\lambda}{d_i}\left[2.514 + 0.8\ exp\left(-0.55\frac{d_i}{\lambda}\right)\right]$; Cunningham slip correction factor for droplet i
C_{Di}	$= \frac{24\left(1+0.11037\sqrt{Re_i}\right)^2}{Re_i\ C_{ci}}$; drag coefficient of droplet i
C_l	specific heat capacity of the liquid ($J\ kg^{-1}\ K^{-1}$)
C_{pg}	specific heat capacity of the gas ($J\ kg^{-1}\ K^{-1}$)
d_i	diameter of droplet i (m)
$\bar{d}$	average droplet diameter at a given z (m)
$\overline{d_0}$	initial average droplet diameter (m)
d_j	jet diameter (m)
D_c	outer capillary tube diameter (m)
d_p	precipitation diameter at which the droplets' evaporation ceases (m)
d_{pro}	progeny diameter (m)
d_R	diameter of a droplet at its Rayleigh limit or critical diameter (m)
$\mathbf{E}'$	electric field due to electrodes and space charge of ions and progenies ($V\ m^{-1}$)
$\mathbf{E}$	electric field due to electrodes and space charge of all charged entities ($V\ m^{-1}$)
f_i	heat transfer correction factor for droplet i
$\mathbf{F}_{Di}$	drag force acting on droplet i (N)
$\mathbf{F}_{Ei}$	electric force acting on droplet i (N)
f_m	mass fraction of a droplet taken away by the progenies in a Coulomb fission event
$\mathbf{g}$	acceleration of gravity vector (= 9.806 $m\ s^{-2}$)

H	capillary tube tip to plate distance (m)
I_o	net ionic electric current emerging from the orifice into the electrospray domain (A)
I_d	current carried by the droplets (A)
I_{ion}	current carried by the ions (A)
$\mathbf{J}_{ion}$	ionic current flux (A m^{-2})
$\mathbf{J}_{pro}$	number flux of progenies (# s^{-1} m^{-2})
k_B	Boltzmann constant
K_{ion}	ion electric mobility (m^2 V^{-1} s^{-1})
K_d	droplet electric mobility (m^2 V^{-1} s^{-1})
K_{pro}	progenies electric mobility (m^2 V^{-1} s^{-1})
l_{TC}	height of the Taylor cone (m)
l_J	jet length before breakup (m)
l_{CR}	vertical distance between the capillary tip and the ring (m)
l_R	height of the ring (m)
L	heat of vaporization of the solvent (J kg^{-1})
m_i	mass of droplet i (kg)
N	number of tracked droplets in the system (#)
N_{pro}	number of progeny droplets created in a Coulomb fission event (#)
n_{pro}	number density of progeny droplets (# m^{-3})
Nu_i	Nusselt number for droplet i
p	pressure (Pa)
Pe_{ion}	$= \frac{q_{ion}\, E\, d_i}{k_B T_g}$; ion's Peclet number near droplet i, ratio between the fluxes due to electric convection and diffusion (q_{ion} is the charge of the ion, here equal to one elementary charge)

p_q	electric charge ratio of the progeny droplet (its charge divided by its Rayleigh limit charge)
Pr_g	Prandtl number for the gas
Q	volumetric flow rate of the sprayed liquid ($m^3\ s^{-1}$)
q_i	electric charge of droplet i (C)
q_{pro}	electric charge of progenies (C)
q_R	Rayleigh limit electric charge (C)
$\overline{q_0}$	Initial average electric charge of the droplets (C)
r	radial coordinate (m)
$\mathbf{R}_i$	$= [x_i, y_i, z_i]$; position vector of droplet i (m)
$\mathbf{R}_I$	$= [x_i, y_i, 2H - z_i]$; position vector of image of droplet i in the plate (m)
$\mathbf{R}_{ij}$	$= \mathbf{R}_i - \mathbf{R_j}$; displacement vector from droplet i to a droplet j (m)
$\mathbf{R}_{iJ}$	$= \mathbf{R}_i - \mathbf{R}_J$; displacement vector from the image of droplet j to droplet i (m)
Re_i	$= \frac{\rho_g u_g d_i}{\mu_g}$; Reynolds number for droplet i
Sc_g	Schmidt number for the gas
Sh_i	Sherwood number for droplet i
t	time (s)
T_i	temperature of droplet i (K)
T_g	temperature of the gas (K)
$\mathbf{u}_g$	gas velocity vector ($m\ s^{-1}$)
$\overline{u_{g0}}$	average gas speed at the upper inlet ($m\ s^{-1}$)
$\mathbf{u}_{ion}$	ionic velocity vector ($m\ s^{-1}$)
$\mathbf{u}_{pro}$	progenies velocity vector ($m\ s^{-1}$)
$\mathbf{V}_i$	velocity vector for droplet i ($m\ s^{-1}$)

V_J	jet velocity (m s^{-1})
z	axial coordinate (m)

Greek Letter Symbols

α	the standard deviation of the initial droplet radial position normalized by the initial average droplet diameter
β	coefficient of variation of the initial droplet diameter distribution
γ	numerical parameter controlling the pseudo-transient method
ε_m	electric permittivity of the surrounding medium, taken as ε_0 for the gas and $2.1\varepsilon_0$ for the dielectric (C V^{-1} m^{-1})
ε_0	electric permittivity of vacuum (C V^{-1} m^{-1})
η_{pro}	specific rate of progeny generation (# m^{-3} s^{-1})
θ	$= C_{pg}/C_l$; ratio of the specific heat capacities
κ	electric conductivity of the liquid (S m^{-1})
λ	mean free path of the gas molecules (6.51×10^{-8} m; Seinfeld & Pandis, 2016)
μ_g	dynamic viscosity of the surrounding gas (kg m^{-1} s^{-1})
μ_l	dynamic viscosity of the liquid (kg m^{-1} s^{-1})
ν	specific charge combination rate of ions with droplets and progenies (C m^{-3} s^{-1})
ρ	charge density generated by droplets, ions, and progenies (C m^{-3})
ρ'	charge density generated by ions and progenies (C m^{-3})
ρ_l	density of the liquid (kg m^{-3})
ρ_g	density of the gas (kg m^{-3})
ρ_{ion}	ions' charge density (C m^{-3})
ρ_{pro}	progenies' charge density (C m^{-3})
ρ_{drop}	droplets' charge density (C m^{-3})
σ	surface tension coefficient (N m^{-1})
τ_i	$= \frac{d_i^2 \varrho_l}{18\,\mu_g}$; relaxation time of droplet i (s)
φ	Taylor cone's semi-angle (rad)
ϕ	electric potential created by the electrodes and the space charge due to all the charged entities (ions, progenies, and droplets) (V)

ϕ_C	voltage at the capillary (V)
ϕ_R	voltage at the ring (V)
ϕ'	electric potential created by the electrodes and the space charge due to the ions and the progenies (V)
ϕ^*	electric potential created by the electrodes in absence of ring (V)

Acronyms

CF	Coulomb fission
TC	Taylor cone

When making micro- and nano-particles by electrospray, CF events lead to undesirable particle morphologies and the widening of the particle size distribution (Bodnár et al., 2018). CF events can usually be prevented by raising the solute concentration, but only within a narrow range of concentrations, which are high enough to make the TC more prone to drying and become unstable (Bodnár et al., 2018). In addition, when collecting dry particles, electrostatic charge buildup could result in particle loss from, and electrical breakdown at, the collection spot (Bodnár and Rosell-Llompart, 2013). Another, less acknowledged issue caused by the high charge is the droplets' high speeds in the spray, which can result in wet particles reaching the counter-electrode due to the short droplet lifetimes. Finally, the scalability of the technology is hampered by the charge repulsion between multiple electrosprays (Bocanegra et al., 2005; Deng and Gomez, 2007; Sochorakis et al., 2019). In conclusion, strategies are broadly needed for the in-situ controlled reduction of the droplet charge in electrosprays.

A promising already tested strategy involves the use of unipolar corona ions of opposite polarity (Yurkstas and Meisenzehl, 1964; Noakes et al., 1989; Meesters et al., 1992; Tang and Gomez, 1994; Rulison and Flagan, 1994; Ijsebaert et al., 2001; Zimlich et al., 2002; Xie et al., 2006; Ciach, 2006; Almería and Gomez, 2014; Tang et al., 2017; Mustika et al., 2021; Carrasco-Munoz et al., 2022; Vu et al., 2023). The efficiency of a corona-electrospray charge reduction process was only experimentally quantified recently by us (Carrasco et al., 2022). In that work, ions from a negative corona discharge were introduced axially and counter-currently to the electrospray, approximately matching the electrospray current. The discharged aerosol was then extracted continuously through an orthogonally-positioned tube, and collected on a filter. With this configuration, and over various compositions, high discharging and filter

sampling efficiencies were demonstrated. Nonetheless, the extracted aerosols still held some residual charge (under 20% of the overall electrospray current), which suggested dissimilar discharging histories for different droplets' trajectories. We also showed that maximizing droplet discharging while minimizing particle losses relies critically on the choice of geometrical and electrostatic parameters.

Clearly, the design optimization of new electrospray-corona devices requires the analysis of many variables, including geometrical parameters, electrodes' voltages, configuration and discharging characteristics of the ion source, gas flow field, etc. Pursuing such optimization experimentally is time-consuming. Therefore, numerical simulations could guide the analysis and selection of different proposals.

The purpose of this article is to develop a model and implement a numerical simulation scheme, to study the process of charge reduction on evaporating electrospray droplets, by means of unipolar ions, with the double aim of (1) preventing CF events and (2) achieving high efficiency of extraction of the neutralized aerosol.

A model for some configurations and the simulations results have recently been proposed by Higuera (2016) and by Khalifehei and Higuera (2020, 2023). Those simulations have captured the main physics for the proposed configurations, although the models neither considered droplet evaporation (thus, without CF events), nor the size polydispersion at droplet generation, nor the possibility of ion transfer to the TC.

The present article is structured as follows. In section 2, we identify the key elements needed to achieve efficient droplets discharging and extraction. In section 3, we present our mathematical model of the different mechanisms and processes involved (section 3.1), and the methodology we used to solve the coupled equations (section 3.2). Finally, in section 4, we present the results of the numerical simulations for various suitable configurations. These simulations were conducted under different flow conditions and for two solvents: acetone and methanol, significantly varying in volatility. We thoroughly analyze the influence of the various key factors on the in-situ droplet discharging.

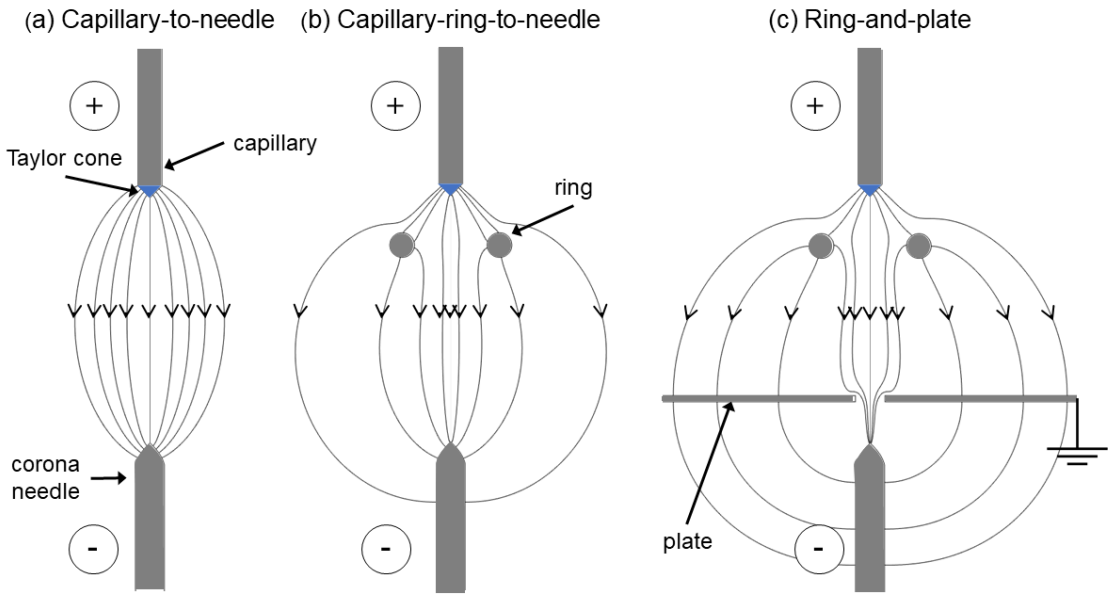

Fig. 1. Three electrostatic configuration options with electric field lines based on an electrospray capillary and a coaxially-arranged needle for corona discharge: (a) both naked, (b) with an intermediate ring electrode close to the capillary, and (c) with a ring plus an Earth-grounded plate close to the corona needle, comprising an orifice for discharging ions (the corona assumed to take place between the corona needle and the plate).

2. Configuration options for efficient droplet discharging

As different configurations have been proposed in the literature, in this section, we theoretically address configurations and strategies needed for an efficient and stable droplet discharging and extraction. Understanding the function of each element is necessary to motivate pertinent questions in the numerical simulations.

Neutralizing a very high fraction of the electrospray droplets in a volatile spray is challenging. This goal should be distinguished from producing neutralized droplets at any rate and any cost, regardless of whether the process is inefficient. A priori, discharging all the droplets in one electrospray by means of corona ions may seem difficult because: (1) the droplets fill a large, oddly shaped spray region, expanding from a small droplet-generation zone near the TC microjet to a macroscopically sized (of order ~1 cm) region; (2) the available time for interaction between a droplet and the ions is very short because the droplets move quite fast, at speeds of several m/s (resulting in droplet lifetimes of the order of 10^{-2} s); and (3) the two types

of charge carriers -the ions and the droplets are generated by different mechanisms, with different overall electric currents, and therefore, also different spatial current flux profiles.

A logical location for ion injection, given the axisymmetry of the electrospray, is at the spray axis. Since both the ions and the droplets follow organized trajectories (Grifoll & Rosell-Llompart, 2014), the ions must be introduced so they will intercept the multitude of droplets' trajectories. A naked corona needle placed on the axis, as shown in Fig. 1(a), would attract the electric field lines which are borne at the electrospray capillary and TC, thus pulling the droplets toward the ions, and vice versa, as intended. However, the corona current greatly exceeds the electrospray current, under typical circumstances. Therefore, in this configuration a large excess of corona ions would reach the TC, destabilizing it. Indeed, the liquid-gas interface at the TC would get significantly discharged, causing a drop in the local electric potential and net charge density, thereby strongly weakening the electric stresses needed to sustain the TC (Taylor, 1964; Fernández de la Mora, 1992; Pantano et al., 1994).

To prevent this issue, an intermediate electrode can be introduced as shown in Fig. 1(b) as "ring". The ring's function is to collect the excess ionic charge, and to prevent its arrival to the TC. This would be achieved by proper adjustment of its electric potential, dimensions, and location. Placing the ring electrode near the electrospray capillary additionally enables the electric fields at the TC cone and at the corona to be independently controlled, and with this function it has been applied in some works (Noakes et al., 1989; Meesters et al., 1992; Tang and Gomez, 1994; Ijsebaert et al., 2001).

Unfortunately, in this configuration charged droplets reach the corona region, where droplets and their decomposition products would poison the corona needle tip (by changing its geometry and electric characteristics). To avoid this issue, a plate electrode placed in front of the corona needle is proposed here, as shown in Fig. 1(c). This element also allows independent control of the field in the droplet discharging region from the field necessary to sustain the corona discharge (Cloupeau, 1994; Tang et al., 2017). A small orifice in the plate allows the passage of ions to the spray region at a desired rate. Additionally, gas can be pushed through the plate orifice (toward the spray region) to discourage the entrance of any droplets or solvent vapors, and to maintain a constant gas composition around the corona.

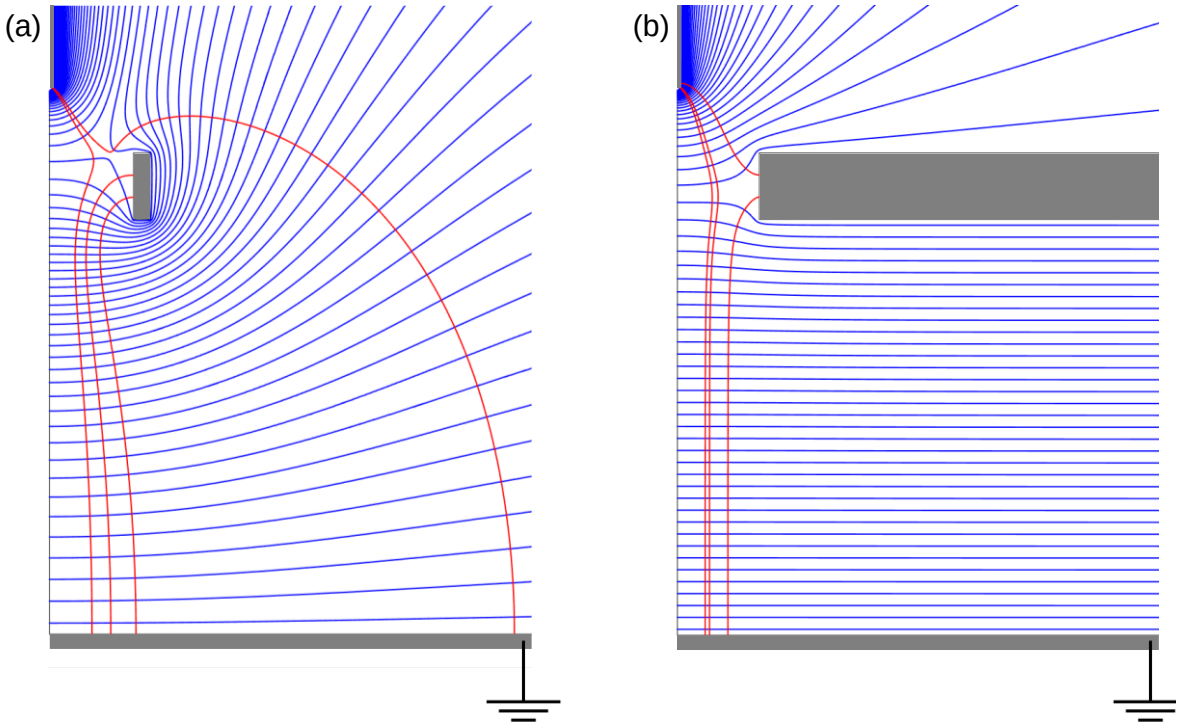

Fig. 2. Electric potential (depicted by blue lines) and selected field lines (depicted by red lines) shown for a basic setup composed of a capillary, a ring, and an Earth-grounded plate, in a rz diagram. The figure showcases two scenarios: (a) with a narrow ring and (b) with a very wide ring. The ring voltage is half of the capillary voltage. In both cases, field lines depart from the same points at the capillary tip and at the inner face of the ring.

In this geometry, the deposition of ions onto the ring can be favored by making the ring thin enough. Fig. 2 compares the field obtained using a very thick or a thin ring. In the latter, the electric field is strongly weakened within the ring, but also above the ring, between it and the TC (Fig. 2(a)). The thinness of the ring makes it possible for the plate to strongly influence the region above the ring, as equipotential lines which are right below the ring are able to wrap around the ring and reach the space atop the ring's hole. This has several effects which help to discourage the transport of ions towards the Taylor cone. One effect is the larger zone of weak field than for a thicker ring. The other is the capturing of excess ions at the ring, preventing their reach of the TC. This is shown in panel (a), in which two field lines (red lines) coming straight up from the plate and turning sharply toward the ring. For the very wide ring shown in panel (b), the effect is much less pronounced.

Besides electrostatic control, a forced gas stream is needed to extract the discharged droplets from the system. In the absence of such a gas flow, the discharged droplets would tend to accumulate in the spray and eventually wander away uncontrollably, as we recently observed

experimentally (Carrasco-Munoz et al., 2022). In such scenario without forced gas flow, gas motion is still induced by the motions of the charged electrospray droplets (Arumugham-Achari et al., 2013) and of the ions (Qu et al., 2021). Analyzing such induced-flow scenarios, however, falls outside our scope here, where only forced gas flows are considered. See Appendix A for additional discussion on this topic.

The weak electric field zone formed within the ring's hole (Fig. 2(a)) prevents the ions from reaching the TC. (That this precisely true will be verified later in the simulations.) However, if the ions were unable to pass through the ring, so would the droplets, unless assisted by a downward gas stream passing through the ring. Such a stream could be chosen to affect the droplets' velocities without noticeably affecting the ions' (as the ions have much greater electric mobility than the droplets). In conclusion, the gas flow is a powerful "control knob" that allows influencing the droplets and the ions differently. The combination of a weak electric field in the ring hole with a downward gas stream helps push the droplets through the ring, with the aim to find the conditions which can lead to efficient droplet discharging on the downstream side of the ring electrode, away from the TC.

Based on the foregoing discussion, our simulations consider the configuration of Fig. 1(c) with a gas flow coflowing downward with the electrospray, which passes through the ring hole and exits the system through a circular slit in the Earth-grounded plate. This axisymmetric configuration is shown in Fig. 3, where the ring has a rectangular section, and is held by a dielectric solid which also confines the gas to pass through the inside of the ring. We have numerically studied the efficacy of this configuration for two different solvent systems, and various gas speeds and ring electrode configurations.

3. Mathematical model and methodology

Section 3.1 gives the equations governing the behavior of the different processes under study, where several of them exhibit coupled physics. Section 3.2 describes the procedures and implementation details needed to solve these governing equations. Variables not defined explicitly can be found in the Nomenclature of the article.

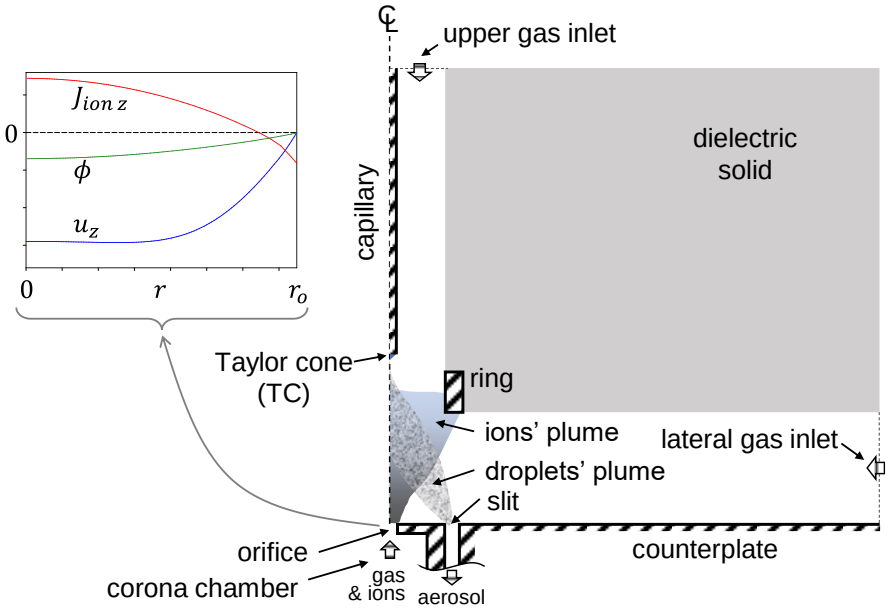

Fig. 3. Sketch of the general system, including its main elements. The graph at the left shows the profiles of gas velocity ($u_{g\,z}$), flux of ions ($J_{ion\,z}$), and potential (ϕ) at the orifice connecting to the corona chamber. These profiles are used as boundary conditions in the simulations. The dielectric solid is introduced to hold the ring and to guide the incoming gas flow.

3.1 Governing equations and boundary conditions

We extend our previous models and implementations for the simulation of electrospray droplets dynamics (Grifoll and Rosell-Llompart, 2012; Arumugham-Achari et al., 2013; Grifoll and Rosell-Llompart, 2014; Arumugham-Achari et al., 2015) to account for ion transport in the gas phase and droplet discharge kinetics.

3.1.1 Droplet dynamics

Two frameworks exist to describe the movement of charged droplets: the Eulerian and the Lagrangian frameworks. The first one is not applicable close to the electrospray injection point (jet breakup region). This is because the droplets created by capillary breakup of a straight jet move nearly axially, and, for a while, occupy a narrow region around the axis. The smallness of this region (especially, its radial dimension which is initially smaller than the inter-droplet distance) precludes the definition of the droplets' number density in that region (Grifoll and

Rosell-Llompart, 2014). Further downstream, where the number density can be defined but is still relatively high, the Eulerian calculation of the droplets' electrostatic interactions requires the use of the rate of change of the distribution function due to collisions (electrostatic interactions), which is generally unknown (Higuera, 2012). Further downstream, as the spray becomes more dilute, such rate of change becomes negligible, allowing a Eulerian description. However, such a description must be implemented downstream of a certain mathematical surface, at which a distribution of the droplets' number density must be assumed as boundary condition (Higuera, 2012).

Here, we have adopted the direct Lagrangian particle dynamics simulation of electrostatic sprays, as described, for instance, by Arumugham-Achari et al. (2015), in which the motion of each droplet i is tracked in the electrospray, subjected to Newton's laws of motion:

$$\frac{d\,\mathbf{R}_i}{d\,t} = \mathbf{V}_i \tag{1.a}$$

$$m_i \frac{d\,\mathbf{V_i}}{d\,t} = \mathbf{F}_{Di} + \mathbf{F}_{Ei} \tag{1.b}$$

where the drag force is computed as

$$\mathbf{F}_{Di} = C_{Di}\frac{\pi}{8} d_i^2 \rho_g \left(\mathbf{u_g} - \mathbf{V}_i\right)\left|\mathbf{u}_g - \mathbf{V}_i\right| \tag{2}$$

where the drag coefficient C_{Di} has been computed as proposed by Abraham (1970) corrected with the Cunningham slip correction factor (Allan and Raabe, 1982; see also the Nomenclature).

The electric force on each droplet $\mathbf{F}_{Ei}$ in Eq. (1.b) is decomposed into a term associated with an external field and another term grouping the interaction with other droplets and the image charges in the plate (assumed infinite), as

$$\mathbf{F}_{Ei} = q_i\mathbf{E}' + \frac{q_i}{4\pi\varepsilon_m}\left[\sum_{j\neq i}^{N} q_j\left(\frac{\mathbf{R}_{ij}}{R_{ij}^3} - \frac{\mathbf{R}_{iJ}}{R_{iJ}^3}\right) - q_i\frac{\mathbf{R}_{iI}}{R_{iI}^3}\right] \tag{3}$$

where $\mathbf{E}'$ is the external electric field due to the electrodes and the charged entities except the droplets (that is, including the ions and the progenies generated in droplet's Coulomb fissions). This expression is a good approximation of the actual force, because it only neglects the contributions due to the charges induced by the droplets on the ring and the capillary (and their

images in the plate, and higher order images), which are negligible (see Appendix A). In previous Lagrangian simulations we applied the so-called Continuous-Charge Submodel (Grifoll and Rosell-Llompart, 2014) where the droplet-droplet electric interactions are accounted for individually only for a small fraction of the droplets, while the others contribute to a mean electric field. Here, however, the presence of ions and progenies in the present problem could jeopardize this methodology. Therefore, all the electric forces between the droplets are accounted for explicitly in Eq. (3).

The electric field $\mathbf{E}'$ is computed by solving Poisson's equation:

$$\nabla \cdot \mathbf{E}' = -\nabla^2 \phi' = \frac{\rho'}{\varepsilon_m} \tag{4}$$

where the space charge density ρ' does not include the charge of the droplets themselves and is thus given by

$$\rho' = \rho_{ion} + \rho_{pro} \tag{5}$$

The boundary conditions for the electric potential ϕ' are Dirichlet for the electrodes (the plate, the ring, and the capillary tube including the TC) where the voltage is known. They are also of this type for the orifice through which the ions enter the electrospray domain, and for the slit through which the droplets exit this domain. On these two open boundaries the potential is given as a function of the radial position, $\phi' = \Psi_O(r)$ for the orifice (Fig. 3) and $\phi' = \Psi_S(r)$ for the slit (see Appendix A). The function $\Psi_O(r)$ was obtained from a simulation of the corona discharge process, as explained later (section 3.2.3). On the other hand, $\Psi_S(r)$ was obtained by solving Laplace's equation for a system consisting of a capillary, a ring, and a plate with a long concentric tube at the slit exit. In this simulation, the plate and the walls of the cylindrical slit were electrically grounded. At the electrostatic open boundaries far from ions and droplets (upper and lateral boundaries in Fig. 3), a Neumann type ($\partial\phi'/\partial n = 0$) boundary condition is enforced. The same boundary condition is also applied at the system axis.

3.1.2 Droplets' evaporation and temperature

The solvent evaporation from droplets containing non-volatile solute species leads to the formation of solid particles. The description of this complex process is beyond the scope of this study (Bodnár et al., 2018). Instead, we let each droplet evaporate as if composed of pure-

solvent until it reaches a precipitation diameter, d_p. From this moment on, evaporation ceases, and the droplet is tracked as a solid spherical particle with constant diameter.

The phenomenon of evaporation of a single-component droplet has been modeled following Arumugham-Achari et al. (2015), where we adopted the model M7 of Miller et al. (1998). In this model, the evolution of the temperature and mass for each droplet is tracked with

$$\frac{d\,T_i}{d\,t} = \frac{f_i\,Nu_i}{3\,Pr_g}\frac{\theta}{\tau_i}\left(T_g - T_i\right) + \frac{L}{C_l}\frac{\dot{m}_i}{m_i} \tag{6}$$

$$\dot{m}_i = \frac{d\,m_i}{d\,t} = -\frac{Sh_i}{3\,Sc_g}\,\frac{m_i}{\tau_i}\ln(1 + B_{Mi}) \tag{7}$$

where the Frössling correlations for heat and mass transfer have been used to estimate the Nusselt and Sherwood numbers (Arumugham-Achari et al., 2015; Sazhin, 2017). We have assumed the temperature of the gas, T_g, to be uniform and constant. This assumption is justified because in a previous Lagrangian simulation of similar electrosprays where only the gas flow induced by the electrospray droplets was considered, the maximum variation of temperature in the gas phase was found to be only 4 ºC (Arumugham-Achari et al., 2015). In the present study, where an external and much larger gas flow rate is applied, much smaller temperature differences are expected.

3.1.3 Coulomb fission events and progeny droplet transport

Several experimental and numerical simulation studies previously reported on the mass and charge released by a droplet in a CF (Hunter and Ray, 2009; Grimm and Beauchamp, 2002, 2005, 2010; Li et al. 2005; Pillai et al., 2016; Singh et al., 2019). Here, the relevant findings of the experimental observations are accounted for by a few simple rules: When the diameter of a droplet reaches the critical Rayleigh limit value,

$$d_R = \left(\frac{q^2}{8\pi^2\varepsilon_0\sigma}\right)^{1/3} \tag{8}$$

a CF event happens instantaneously. Such an event is modeled by considering that the parent droplet ejects a certain number of progeny droplets (N_{pro}), which reduces the parent's mass by a fraction f_m, taken as constant, while the charge carried by each progeny is a given fraction p_q of its own Rayleigh limit.

Because of the potentially large number of progeny droplets in the system, we do not keep track of them individually. Instead, we model them as a continuous cloud transported convectively and electrophoretically (neglecting droplet inertia). The number density of this cloud, n_{pro}, follows the Eulerian conservation equation in which the rate of progeny generation per unit volume η_{pro} (source term) is equaled to the divergence of the number flux of progenies $\mathbf{J}_{pro} = \mathbf{u}_{pro} n_{pro}$:

$$\eta_{pro} = \nabla \cdot \mathbf{J}_{pro} \tag{9}$$

where the velocity of the progenies is given as

$$\mathbf{u}_{pro} = \mathbf{u}_g + K_{pro}\,\mathbf{E} \tag{10}$$

In Eq. (10) the electric mobility is estimated as (Hinds, 1999)

$$K_{pro} = q_{pro}\, B_{pro} \tag{11}$$

where the constant mechanical mobility coefficient, $B_{pro} = \left(3\,\pi \mu_g d_{pro}\right)^{-1}$, is computed from the properties of the progenies. Note that Eq. (9) does not consider time derivatives; therefore, during the transients, its numerical solutions cannot be interpreted as real, and only gain physical sense after a statistically steady state is reached. When solving Eq. (9) $n_{pro} = 0$ at the gas inlet boundaries (Fig. 3). In addition, progeny droplets reaching any solid boundaries are allowed to "pass through" and disappear.

In Eq. (10) the electric field (**E**) is the mean field computed by solving Poisson's equation for the electric potential (ϕ):

$$\nabla \cdot \mathbf{E} = -\nabla^2 \phi = \frac{\rho}{\varepsilon_m} \tag{12}$$

where the space charge density ρ gathers all charged entities, as

$$\rho = \rho_{ion} + \rho_{pro} + \rho_{drop} \tag{13}$$

The boundary conditions for Eq. (12) are the same as for Eq. (4), as given in section 3.1.1.

3.1.4 Ion transport and discharge rate kinetics

The transport of ions in the system is governed by the Eulerian conservation equation for the ion charge density ρ_{ion},

$$\frac{\partial \rho_{ion}}{\partial t} = -\nabla \cdot \mathbf{J}_{ion} + \nu \tag{14}$$

with flux $\mathbf{J}_{ion} = \mathbf{u}_{ion}\rho_{ion}$, by considering the ion velocity in convective-electrophoresis

$$\mathbf{u}_{ion} = \mathbf{u}_g + K_{ion}\mathbf{E} \tag{15}$$

where $K_{ion}\mathbf{E}$ is the electrophoretic component. The term ν (C/m^3 s) is the specific charge combination rate of ions with droplets and progenies. When the droplets move in regions of large electric field strength, the main discharging mechanism is field discharging (Pauthenier and Moreau-Hanot, 1932). In this mechanism, a continuum of ions moves relative to the droplet, under the action of an external field. Ions passing close enough to the droplet (considered a perfect conductor) impinge on it, under the forces between the ion and the droplet's surface charges. On the other hand, the external electric field around each droplet can weaken to a point where diffusion discharging could become relevant. Therefore, to include both discharging mechanisms, ν has been computed following Lawless (1996), whose equation covers all situations from diffusion discharging (at low ion's Peclet number, Pe_{ion}) to field discharging (at high Pe_{ion}).

The boundary conditions for Eq. (14) are the ion flux at the orifice as a function of the radial position $J_{ion\,z} = \Theta(r)$. The function $\Theta(r)$ was obtained from the (separate) simulation of the corona discharge process, as explained in section 3.2.3 and given in Appendix A. In addition, the ions reaching any solid boundaries are allowed to "pass through" and disappear.

3.1.5 Gas velocity field

The gas velocity field has been computed by solving the steady-state Navier-Stokes momentum conservation equation:

$$\rho_g(\mathbf{u}_g \cdot \nabla)\mathbf{u}_g = \nabla \cdot \left[-p\mathbf{I} + \mu_g\left(\nabla\mathbf{u}_g + (\nabla\mathbf{u}_g)^T\right)\right] + \rho_g\mathbf{g} \tag{16}$$

This equation assumes isothermal and incompressible gas motion, and is coupled to the mass conservation equation:

$$\rho_g \nabla \cdot \mathbf{u}_g = 0 \tag{17}$$

Equation (16) assumes one-way coupling between the gas and the other entities; that is, although droplets, ions, and progenies exert a reactive force on the gas flow (Arumugham-Achari et al., 2013), we neglect such forces due to the dominance of the imposed external flow.

The boundary condition for Eq. (16) is $\mathbf{u}_g = \mathbf{0}$ at all solid boundaries. At the upper gas inlet (Fig. 3), a velocity profile for a Poiseuille flow between concentric cylinders was imposed. At the ions' orifice, the gas velocity boundary condition was the radial profile which was obtained from the simulation of the corona discharge process, explained later in section 3.2.3. At the lateral gas inlet, a normal velocity condition was imposed. Finally, past the slit on the plate, the gas followed a long path before exiting the system with a Poiseuille-flow velocity profile between concentric cylinders.

3.2 Methodology and implementation details

Each simulation was conducted in two stages. First, the evolution of the droplet spray was computed without the presence of ions until a pseudo-steady state was achieved. Then, the ions were introduced, and the system was allowed to evolve further until a new pseudo-steady state was attained (see Appendix A). We describe here the electric field computations, the rules of droplet injection, the ion generation model, and the simulation in the corona chamber. The solution of the corona simulation was used to determine the boundary conditions at the orifice exit for the ion transport and for electric field in the spray domain. Such simulation (section 3.2.3) and the gas dynamics simulation in the spray chamber (section 3.1.5) were solved using COMSOL Multiphysics® (2016) in a two-dimensional cylindrical coordinate system.

3.2.1 Electric field computations

As described in 3.1.1 and 3.1.3, the computations of the electric fields ($\mathbf{E}'$ and $\mathbf{E}$) require the charge densities of the droplets, progenies, and ions. An exhaustive simulation should involve the integration, at each time step, of the droplet's equations of motions and of Poisson's equations for the electric fields $\mathbf{E}$ and $\mathbf{E}'$ (Eqs. 12 and 4). To alleviate the burden of computing such fields, we update them every several integration timesteps, keeping their value constant between updates. This does not impact the accuracy of the steady state solution, because at that point the electric field practically does not change with time, as the clouds of charged entities rearrange only slightly (Grifoll and Rosell-Llompart, 2014).

The timescale used to solve the movement of the droplets is inadequate for solving the transport of ions, which move much faster. Therefore, using the same integration time step for solving the ions transport equation leads to numerical instabilities. We suppress these instabilities by using a pseudo-transient method (Fletcher, 2005), which involves solving, instead of Eq. (14), the equation:

$$\gamma \frac{\partial \rho_{ion}}{\partial t} = -\nabla \cdot \mathbf{J}_{ion} - \nu \tag{18}$$

where the value of the parameter γ (=300) has been empirically selected to assure a stable evolution toward the steady state. As the solution approaches steady state ($\partial \rho_{ion}/\partial t = 0$), it converges to the solution of Eq. (14).

3.2.2 Introduction of the droplets into the system

The TC at the tip of the capillary has a height $l_{TC} = 0.5\, D_C/tan(\varphi)$, where φ is the cone semi-angle and D_C is the external diameter of the capillary. The capillary and the cone share the same electric potential (Pantano et al., 1994). From the tip of the cone emanates a jet, whose length l_J has been estimated following Ismail et al. (2018), who distinguish two cases: high and low electric Reynolds number: $\left[\left(\rho_l^5 Q^3 \sigma \kappa\right)/(\mu_l \varepsilon_0)\right]^{1/6} > 5$ or < 5. In our simulations, this Reynolds number is greater than 5 and l_J is computed as (Montanero and Gañán-Calvo, 2020)

$$l_J = \frac{42}{\left[\left(\frac{\sigma^5 \varepsilon_0}{\rho_l^5 Q^9 \kappa}\right)^{1/6} - \frac{1}{4\pi}\left(\frac{\sigma \kappa}{\rho_l Q^3 \varepsilon_0}\right)^{1/3}\right]^{1/2}} \tag{19}$$

To avoid complex modelling of the fluid dynamics of the jet, while retaining its electrostatic contribution to the electric field, we mimic the jet as a train of droplets injected from the cusp of the TC (at l_{TC} from the capillary exit) with the constant velocity $V_J = 4\, Q/\left(\pi d_J^2\right)$, where the diameter of the jet, d_J, is estimated as $\overline{d_0}/1.89$ (Rayleigh jet breakup). Except in the jet section itself, the line of charged (moving) droplets generates an electric field which resembles the one that a real jet would create. When the droplets reach the theoretical location of the jet breakup (at $z = l_{TC} + l_J$) the droplets are assigned an initial (x, y)-position, defined by random angular and radial positions. The latter are obtained from a Gaussian distribution with zero

mean and standard deviation $\alpha\overline{d_0}$. From the initial position forward, the droplets' trajectories are governed by equations (1.a) and (1.b) (Grifoll and Rosell-Llompart, 2012).

The diameters of the droplets generated at the tip of the cone follow a lognormal distribution with variation coefficient β. Their electric charge is a fixed fraction of their individual Rayleigh limit charge. Such fraction is such that the initial electric current of the droplets matches the value given by the scaling-laws of Gañán-Calvo et al. (1997).

3.2.3 Ion generation by corona discharge

In the corona discharge simulation, monovalent ions are created in a corona discharge chamber beneath the Earth-grounded plate. In this chamber, a negatively charged needle is coaxially positioned with its tip facing the orifice (see Fig. 1(c) and Appendix A). Air enters this chamber and exits through the orifice into the electrospray domain. In a real system, this gas flow renews the chemical species, and prevents droplets from entering the corona discharge chamber.

The corona discharge process was simulated before the electrospray simulations reported in this article. It was simulated by solving the coupled steady-state problem of ion transport and electric field in a domain composed of the corona chamber, the outlet orifice, and a region above the outlet orifice. This region was upper bounded by a constant-z surface set with a representative potential distribution. Such distribution was derived from iterative electrospray and corona discharge simulations until the solutions converged to the same distribution. These simulations were performed for a representative system, and the resulting ion current flux, electric field, and gas velocity field at the orifice exit plane were subsequently taken as boundary conditions for all the electrospray simulations presented in this study (see Fig. 3 and Appendix A). Using the same boundary condition for all the simulations is acceptable because both the ion generation and transport to the small orifice are very weakly coupled with what takes place in the electrospray domain above the orifice.

More details of these corona simulations are given in Appendix A. A relevant fraction of the ions ended up on the orifice wall and on the plate outside the orifice. For all subsequent electrospray simulations, the ionic current emerging from the outlet orifice into the electrospray domain was the same, but a fraction deposited on the plate (the "fly-back current") which varied depending on the conditions in the electrospray domain (particularly, the electric field), thus changing the portion of ions which travelled upwards towards the ring.

The mathematical model for ion generation in the corona simulations was adapted from the proposal of Adamiak and Atten (2004) and Adamiak et al. (2005). An ion concentration distribution at the surface of the needle tip was initially selected and the coupled equations for ion transport and electric field were solved. The electric field strength was then computed along the needle's tip surface and compared to the field strength given by Peek's equation (Zhang et al., 2007). If they were different, new ion concentration values were assigned at the tip, and the ion transport and the electric field were computed again. This iterative process was continued until the resulting electric field strength differed negligibly from the one calculated from Peek's equation. See Appendix A for more details.

Although our simulations are not dependent on electric polarity, formally we have adopted negative ionic polarity. Experimentally, we have found negative coronas to be stable and convenient to use for this purpose (Carrasco-Munoz et al., 2022).

3.2.4 Numerical scheme for transport and droplet transformations

The equations for the droplet movement (Eqs. 1.a and 1.b) were integrated using small time steps, Δt, using the Ermak integration scheme (Ermak and Buckholz, 1980; Grifoll and Rosell-Llompart, 2012). After each time step, the size and the charge of each droplet were updated to account for the mass loss due to solvent evaporation, and the charge loss due to ionic capture. When the Rayleigh limit of a droplet was exceeded, a CF event was declared, and the droplet's mass and charge were reduced by the rules given in section 3.1.3, and the ejected amounts transferred to the progenies.

The transports of the progeny droplets and the ions were simulated in a dense 2D cylindrical coordinates grid (as described in Arumugham-Achari et al., 2015). Equations (9) and (18) were discretized using a finite-volume formulation with an upwind scheme for the convective term (explicitly integrated with respect to time). At each time step, the specific rate of progeny droplets generation (η_{pro}) was computed in each grid cell, by accounting for the number of CF events, the number of progenies released in each event, the cell volume, and Δt. In Eq. (18), the specific discharge rate (ν) was computed in an analogous way by accounting for the discharging suffered by the droplets and the progenies in a Δt.

4. Results

Section 4.1 provides an overview of the relevant system features, including the electrode potential selection process to ensure a stable operation of the Taylor cone. In section 4.2, the simulations conducted without ion injection are presented when acetone is the solvent. These results are compared in section 4.3 with those from the simulations with ion injection through the orifice. Finally, in section 4.4 we examine the case when a less volatile solvent, methanol, is used, and compare it to the case of acetone.

4.1 System's characteristics

In experimental work where particles are made by electrospray and collected on a plate, the plate is kept a few cm (two or more) away from the capillary to allow complete droplet drying. One of the questions addressed in our simulations is whether such a typical capillary-to-plate separation is adequate for the corona ions to neutralize the droplets. In addition, the ring electrode (simply "ring") must be sized and positioned without intercepting the electrospray. As the spray is rapidly expanding, the ring's inner radius must be of the order of its distance to the point of emission of the drops. At the same time, its separation from the capillary must be small compared to the ring-to-plate distance, so that the cone-jet can be governed independently by the potential difference between the capillary and the ring.

The ring's dimensions (radial width and axial height) strongly influence the electric field near the ring. In a radially narrow ring (Fig. 2 (a)) the plate has a strong influence on the field in the region between the capillary and the ring, forming a weak-field region located axially above the ring, and radially within the ring (see also Section 2). This weak-field region is desirable as it is an electrostatic barrier for both droplets toward the ring and the ions toward the TC (see Section 2). As will be shown later, the airflow in this region encourages the droplets to move axially down through the ring's hole. The height of the ring, on the other hand, has a strong effect on the intensity of the field inside the ring's hole, where, in the limit case of a tall ring becoming a long tube, the field inside would become very weak. Any droplets and ions entering such a ring's hole would electrostatically precipitate on the inner walls of the ring driven by space charge repulsion. In the other limit of a short and thin ring (small ratios of ring's height to both its inner and outer radii, and its distance to the capillary) the shielding of the plate would weaken inside the ring, with a strengthening of the electric field (see Fig. SI-15 in Appendix

A). Consequently, the ions would be able to arrive at the cone, a scenario which should be avoided. Therefore, there is an optimum between short and tall rings.

For a given system's geometry, the appropriate voltages for the capillary ϕ_C and the ring ϕ_R are selected by meeting two requirements: (i) The electric field strength at the capillary tip must be appropriate to sustain the cone-jet mode, and further downstream, (ii) the electric field must deflect ions away from the TC and toward the ring, as was discussed in section 2 in the context

Table 1. Electrospray system parameters and solvents properties

	Acetone	Methanol
Capillary potential, ϕ_C (V)	5612	5531
Ring potential, ϕ_R (V)	2806	2765
Ring height (mm)	2, 4, 8	2, 4
Average air velocity at the upper inlet, $\overline{u_{g0}}$ (m s^{-1})	1, 2, 4	0.5, 2
Jet length, l_J (mm)	0.729	1.10
Liquid density at 25°C, ρ_l (kg m^{-3})	784.5	789.5
Volumetric liquid flow rate, Q (m^3 s^{-1})[a]	2.06×10^{-10}	2.49×10^{-10}
Surface tension at 25°C, σ (N m^{-1})	22.7×10^{-3}	22.1×10^{-3}
Vapor pressure at 25°C (Pa)	30600	16941
Heat capacity of the liquid at 25ºC, C_l (J kg^{-1} K^{-1})	2160	2539
Droplet's initial charge as percentage of its Rayleigh limit[b]	60.6%	67.1%
Average air speed through the orifice (m s^{-1})	0.50	
Capillary diameter, D_C (mm)	0.50	
Capillary tip to plate distance, H (mm)	33	
Capillary tip to ring vertical distance, l_{CR} (mm)	4	
Ring inner and outer diameter (mm)	10 and 12	
Droplet diameter, count mean, $\overline{d_o}$ (μm)	8	
Diameter of the orifice through which ions enter to the electrospray chamber, 2 r_0 (mm)	3.0	
Ion mobility, K_{ion} (m^2 V^{-1} s^{-1})[c]	-2.3×10^{-4}	
Air background temperature, T_g (°C)	20.0	
Initial droplet temperature (°C)	20.0	
Precipitation diameter, d_p (μm)	2.9	
Fraction of the parent droplet mass taken by the progenies in a CF event, f_m	0.020	

Progenies charge as a percentage of their Rayleigh limit charge, p_q	70%
Number of progenies ejected in a CF event, N_{pro}	4
Ratio between the standard deviation of the initial droplet radius and the average droplet diameter, α	0.15
Coefficient of variation of the droplet diameter distribution, β	0.05
Parameter that controls the pseudo-transient numerical method, γ	300
Net electric current emerging from the orifice to the electrospray domain, I_o (A)	4.0×10^{-7}

[a] Operational volumetric flow rate used by Arumugham-Achari et al. (2015).
[b] With these percentages the spray electric current matches the values used by Arumugham-Achari et al. (2015): 42 and 55 nA, respectively.
[c] Adamiak and Atten (2004).

of Fig. 2. The electric field should also help prevent charged droplets from reaching the ring. To meet the first requirement, we apply the following procedure, which introduces a ring in a capillary-plate system without debilitating the field at the TC. We first estimate the onset voltage ϕ_C^* for a capillary and plate system, using Smith's semi-empirical approach (Smith, 1986). We then determine the potential on the z-axis where the ring will be located later, $\phi_R^* \equiv \phi^*(z = l_{CR})$. This is determined by numerically solving Laplace's equation using COMSOL. We hypothesize that applying $\phi_C - \phi_R = \phi_C^* - \phi_R^*$ ensures the electrical conditions which are necessary for stable cone-jet mode operation in the presence of a ring. This condition on the voltages leaves a degree of freedom in their selection. Solution of Laplace's equation for the capillary-ring-plate system showed that at the additional condition of $\phi_R \sim \phi_C/2$ the electric field directs most ions towards the ring and makes it difficult for the droplets to reach it. This effect is reinforced as the ratio ϕ_R/ϕ_C increases (towards unity), at the expense of increasing both potentials (which is not desirable in practice). As the ratio increases the equipotential lines that come from under the ring (at a value slightly below ϕ_R) wrap around the ring and penetrate more into the space between the capillary and the ring, thus weakening the field in that region, as Fig. 2(a) illustrates (see also Appendix A). The chosen value of ϕ_R/ϕ_C = 0.5 represents a compromise, rather than a value reached through any optimization.

The chosen gas is dry air at normal temperature and pressure conditions. Table 1 specifies the air flow rates in terms of average speeds at the upper gas inlet (Fig. 3). To prevent the lateral

migration of uncharged or low-charged droplets or progenies, and to ensure they exited through the extraction slit, a gentle flow enters through the lateral inlet (Fig. 3). This is achieved by specifying the flow rate at the extraction slit as slightly higher (by 10%) than the sum of the upper-inlet and orifice gas flow rates. A gas flow pattern is shown in Fig. 4.

Regarding the choice of solvents, acetone is of considerable interest because it is non-toxic and highly volatile, thus useful to make dried particles. This high volatility also leads to the early occurrence of CF events (as will be shown). For comparison, a less volatile solvent, methanol, has also been included in this study.

Finally, the evaporation of the droplets is stopped when their volume becomes lower than 1/20 of the volume of a droplet with the initial average-diameter. This simulates a final "dry particle" with a diameter d_p of 2.9 µm. The 1/20 factor corresponds to an initial solute concentration of 5% by volume if the dry particles are compact. This concentration is within the range of normal practice in the field (Bodnár et al., 2018).

Table 1 collects all the important parameters which define the systems studied here, namely solvent properties, system dimensions, and electrospray conditions.

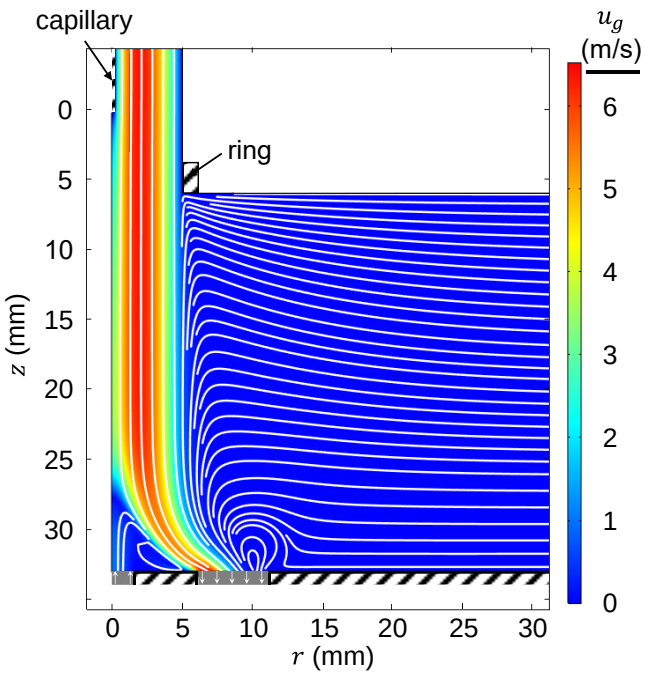

Fig. 4. Streamlines and modulus of the velocity vector (or speed) for a system with an upper-inlet air speed $\overline{u_{g0}}$ of 4 m/s and a ring height l_R of 2 mm. The average air speed through the orifice is 0.5 m/s. The volumetric flow rate at the extraction slit is 10% higher than that coming from the upper gas inlet and the orifice.

4.2 Simulations without droplet discharging (acetone sprays without ions)

Simulations without ions were used as the starting point for the simulations with ions (see Appendix A). In these simulations, which were carried until reaching the steady state, CF events took place extensively. An example for acetone and 2 m/s upper-inlet gas speed is shown in Fig. 5. Panel (a) shows the density of the local rate of CFs (# m^{-3} s^{-1}), as well as a snapshot of the droplets' (r, z) positions, for reference. The snapshot shows that the spray envelope (the outermost droplet trajectory) cuts the equipotential lines at ~90 degrees. This indicates that the droplets follow the electric field lines better than the gas streamlines because their electric mobility remains high despite the loss of charge through CF, such that the droplets' speed $V \sim K_d E \gg u_g$. Panel (b) shows the local rate of CF by the event order (s = 1, 2, … 6), revealing u-shaped zones, which overlap in part. The thinning of the 5th and 6th fission zones is due to the freezing of the evaporation process as the droplets reach the dry particle diameter of 2.9 µm.

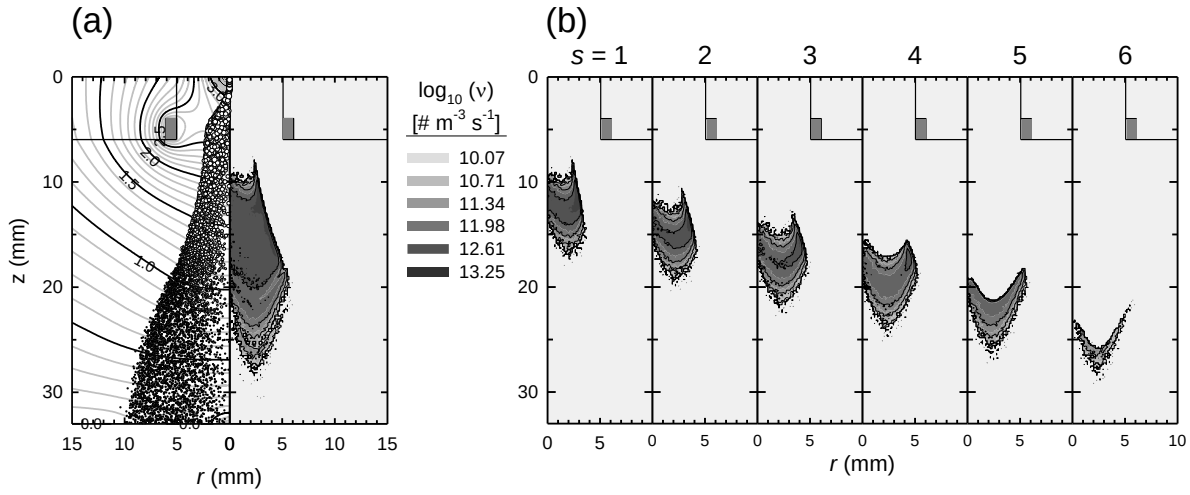

Fig. 5. Droplets' snapshot and Coulomb fissions rate density for an acetone electrospray for a 2 mm ring height and an upper-inlet gas speed of 2 m/s. Panel (a) left: equipotential lines (in kV) and snapshot of the droplets. Panel (a) right shows the fissions rate density for all the Coulomb events and panel (b), for each of the sequential events *s* (=1, …6). In panel (a) the 3D droplets positions are projected into a (r, z) cylindrical coordinate system and the droplets' circles are sized in proportion to each droplet's diameter.

Figure 6 shows the spray snapshots for two gas flow rates and two ring heights. Increasing the gas flow rate causes the spray plumes to become thinner. The widening of the plumes develops in two stages: above and in the ring's hole, and downstream of it. Initially, all four sprays are similar (say, for $z \leq$ 3 mm). However, as the spray approaches the ring and enters inside the ring's hole, the spray stays more focused when the air speed is higher. In this region the electric field weakens (where the equipotential lines are farther apart), and the droplets are transported dominantly by convection. In the case of a "tall" ring, depicted in panel (b), the electric field weakens more than it does for the short ring in panel (a). Near the ring the gas speed is low, and consequently the droplets decelerate enough to reverse their motion, which creates a horn feature that causes them to move towards a point above the ring on the dielectric. Once these droplets reach the dielectric, they are eliminated from the simulation.

The widening of the plumes also develops downstream of the ring. Due to the dynamics taking place above the ring and inside the ring's hole, the spray plumes exiting the ring (z ~ 8 mm) are significantly wider for the lower air speed conditions. Beyond this position, the plumes for the slower air experience extensive droplet CF events which reduce the mobility of the droplets, and cause them to slow down axially, as the electrophoretic component of the velocity is reduced (in a roughly similar electric field strength). This causes the droplets to spend more time to advance axially, and thus expand radially more, driven by space charge repulsion.

4.3 Simulations with droplet discharging (acetone sprays with ions)

When ions are admitted in the system, the spray plumes become significantly narrower, as shown in Fig. 7. The radial component of the electric field is reduced because, due to the ion capture by the droplets, the space charge in the spray is reduced (as demonstrated by the current profiles to be discussed later in this section). Thereby the electrostatic expansion of the spray plume is reduced. Note that the space charge in the system is mostly the droplets' charge, as the ionic charge density is comparatively much lower because the ions move much faster. The direct contribution of the ions to the space charge is only high near the orifice. Nonetheless, the ions have a huge indirect impact on the space charge of the spray by discharging the droplets. The presence of the ions causes a noticeable upwards shifting of the equipotential lines, as can be seen by comparing the shape of the 0.5 and 1.0 kV equipotential lines between Fig. 7 and 6. This shows that the spray expansion in this region in Fig. 6 is mainly due to the space charge forces.

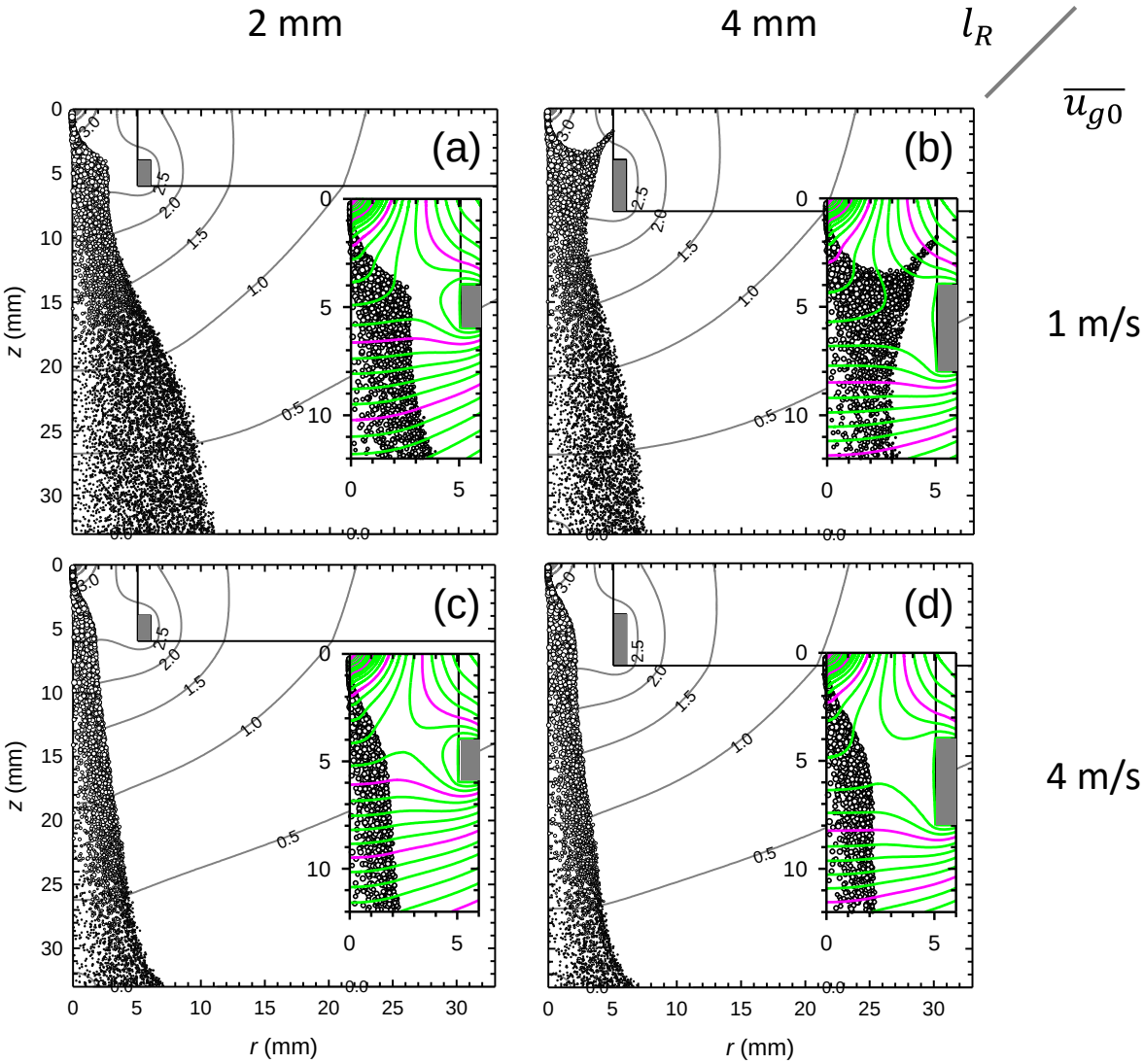

Fig. 6. Simulations without ions. Acetone droplets' snapshot and equipotential lines for an upper-inlet gas speed of 1 m/s (a, b) and 4 m/s (c, d), and for ring height of 2 mm (a, c) and 4 mm (b, d), for equal axial separation between the top of the ring and the capillary. The 3D droplets positions are projected into a (r, z) cylindrical coordinate system, and are depicted as circles of size proportional to the droplets' diameter. The insets show detailed equipotential lines in the zone close to the capillary tip and the ring. The purple lines are the same equipotential lines shown in the main panels (potential values shown in kV). The potential difference between consecutive lines is 100 V.

1

2

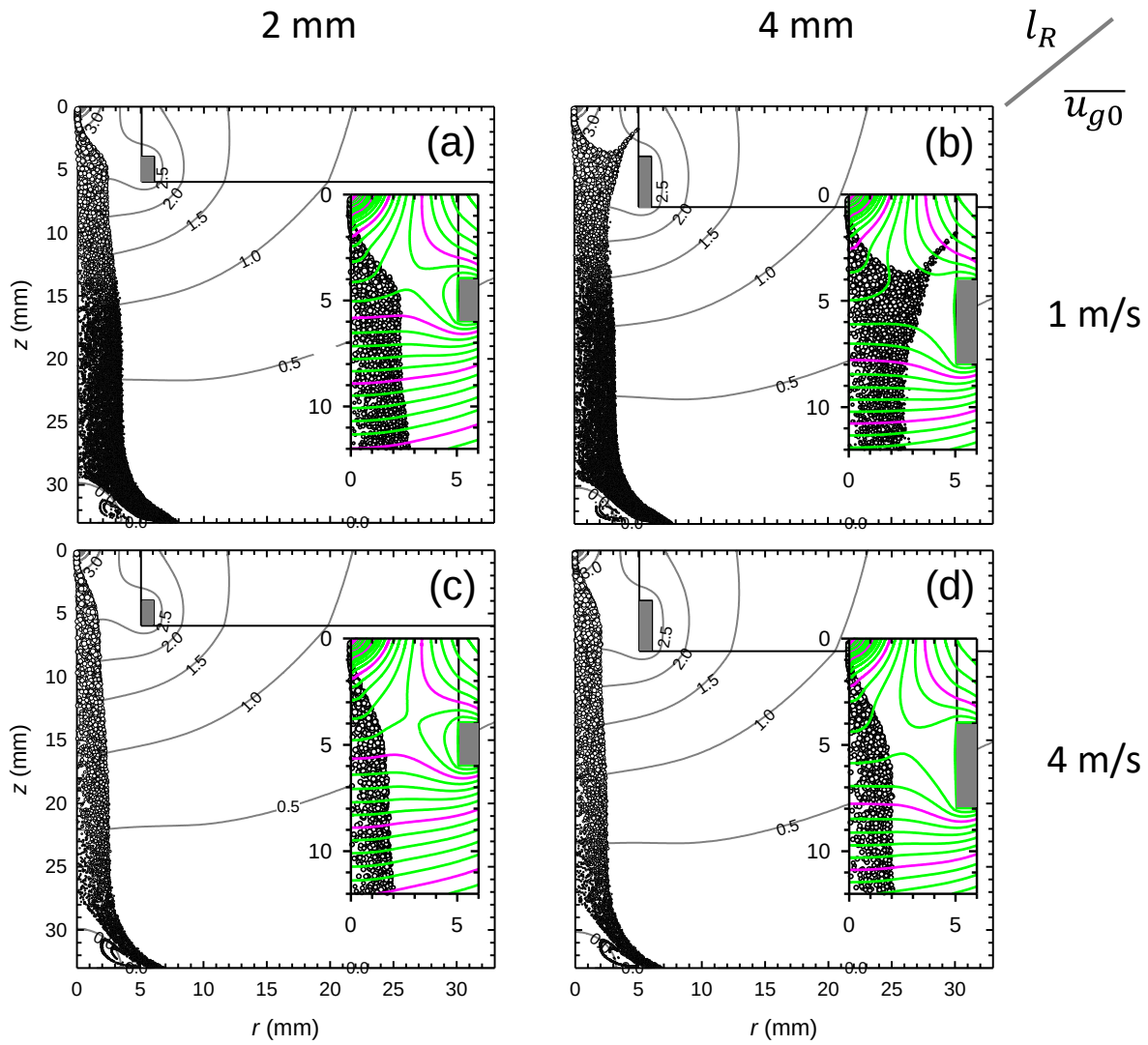

Fig. 7. Simulations with ions. Acetone droplets' snapshot and equipotential lines for a coaxial gas flow of 1 m/s (panels a, b) and 4 m/s (c, d) and for ring height of 2 mm (a, c) and 4 mm (b, d). The droplet's symbol size is proportional to the droplet diameter. The droplets' 3D-positions are projected into a (r, z) cylindrical coordinate system. The insets show detailed equipotential lines in the zone close to the capillary tip and the ring. The purple lines are the same equipotential lines shown in the main panels. The potential difference between consecutive lines is 100 V (potential values shown in kV). The spray plume widths are reduced significantly relative to the case without ions (Fig. 6).

Another consequence of the droplets' charge reduction by ion capture was the complete elimination of CF's for the conditions of panels (a), (c), and (d) of Fig. 7. For the least favorable case of panel (b) (tall ring and low gas speed), the CF events rate was zero everywhere except for droplets flying back above the ring (which give rise to the horn-shaped feature). In this region above the ring, the CF rate was similar with or without ions. This fact and the negligible effect of the ions' presence on the equipotential lines and spray plume shape between the ring

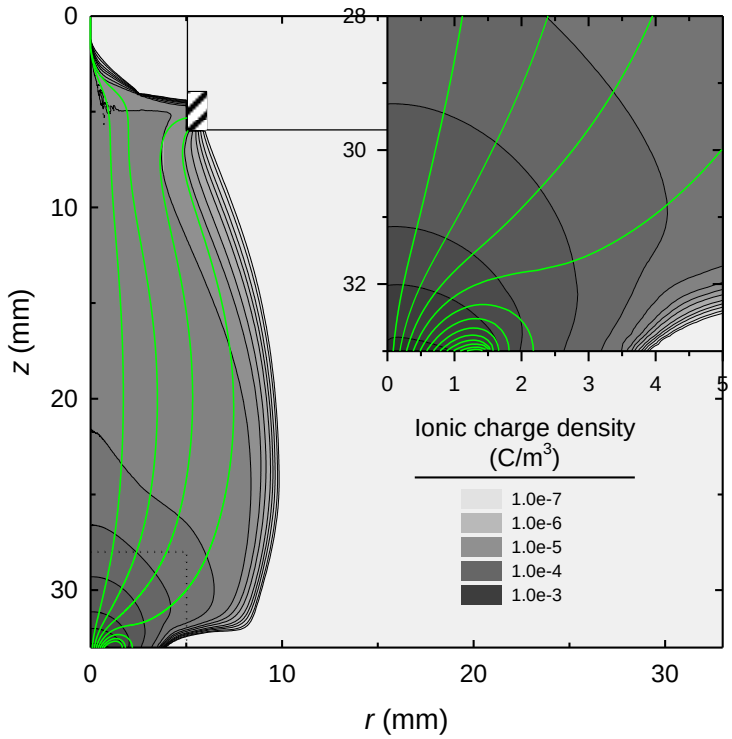

Fig. 8. Ionic charge density ρ_{ion} and ion trajectories for the electrospray system with an upper-inlet gas speed of 4 m/s and ring height of 2 mm. The trajectories correspond to ions released at the orifice at intervals of 0.1 mm. Trajectories were calculated from $\mathbf{u}_{ion} = \mathbf{u}_g + K_{ion}\,\boldsymbol{E}$. The inset is a zoom in the region with dots at the border on the main plot. The orifice radius is 1.5 mm. An important fraction of the ions flies back toward either the top of the plate or the orifice.

and the capillary, indicate electrical decoupling between this region and the region between the ring and the plate.

The space charge associated with the ions is shown in Fig. 8 for the case of upper-inlet gas speed of 4 m/s and ring height of 2 mm. This figure also shows ion trajectories released from the orifice at uniform radial intervals. Between the plate and the ring, the ion cloud fills the entire electrospray region (Fig. 7(c)), a prerequisite for the complete discharging of the spray.

The ionic charge density decreases gradually from the orifice to the ring, and the ions do not penetrate significantly beyond the ring. A few mm above the orifice ($31 \lesssim z < 33\ mm$) the ions suffer a strong radial expansion due to electrostatic repulsion caused by their own space charge (high ionic charge concentration). Such expansion is visible both in the distribution of ionic charge density and in the ion trajectories. The central trajectories for which $r \leq 0.44$ mm at the orifice exit go up toward the upper electrodes. The two leftmost trajectories reach the TC. Although this is not desired, the ionic electric current reaching the TC is negligible, as will

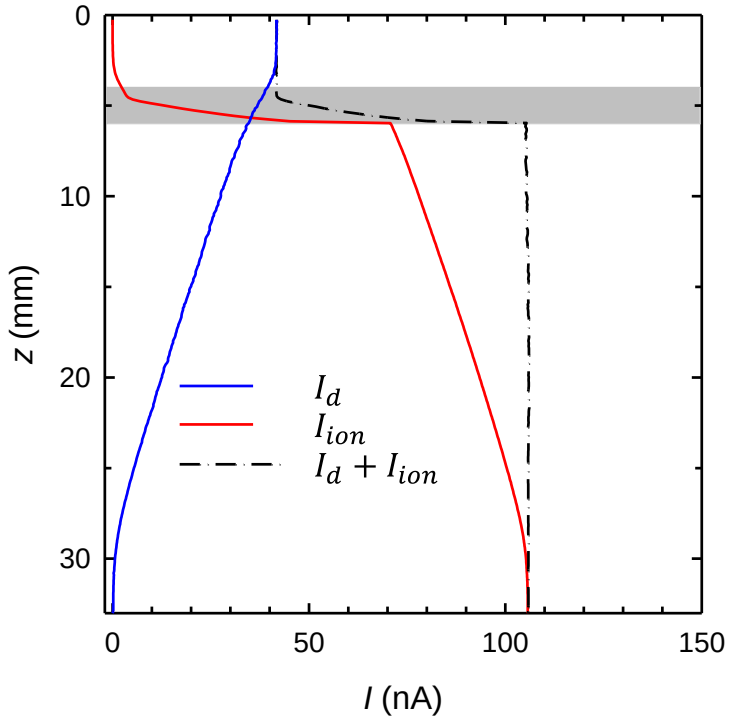

Fig. 9. Electric currents for the droplets and the ions versus z for the system with acetone as solvent, coaxial gas flow of 4 m/s, and ring height of 2 mm. The gray ribbon shows the position of the ring in z. The blue line indicates the current due to the droplets, I_d, the red line is the current due to the ions, I_{ion}. The dashed-dotted line is the overall current (sum of I_d and I_{ion}) which remains constant between the base of the ring (z = 6 mm) and the plate (z = 33 mm), as expected, while the droplets and ions exchange charge, and decreases between z = 6 and 4 mm as ions reach the ring. The ionic current becomes negligible before reaching the Taylor cone.

be shown later. The trajectories within $0.44 < r < 1.12$ mm (orifice exit) have a large slope, and then turn around sharply to land on the upper face of the plate. This trajectory reversal is akin to the so-called flyback of electrospray droplets, also driven by space charge (Bocanegra et al., 2005; Deng and Gomez, 2007; Higuera, 2016; Carrasco-Munoz et al., 2022). Interestingly, the outermost trajectories within $1.12 < r < 1.30$ mm also turn sharply, returning to the orifice, thus contributing a negative ion flux ($J_{ion\,z} < 0$) within $1.30 < r < 1.5$ mm (see Fig. 3).

The electric current associated with the ion flyback reaching the upper face of the plate is a large fraction (74%) of the net ionic current exiting the orifice. Thus, the ion flyback introduces a useful feature: That of providing an "ion reservoir" wherefrom ions can be retrieved on demand by means of the potential difference between plate and ring (as we showed in an experimental study with a similar configuration; Carrasco-Munoz et al., 2022).

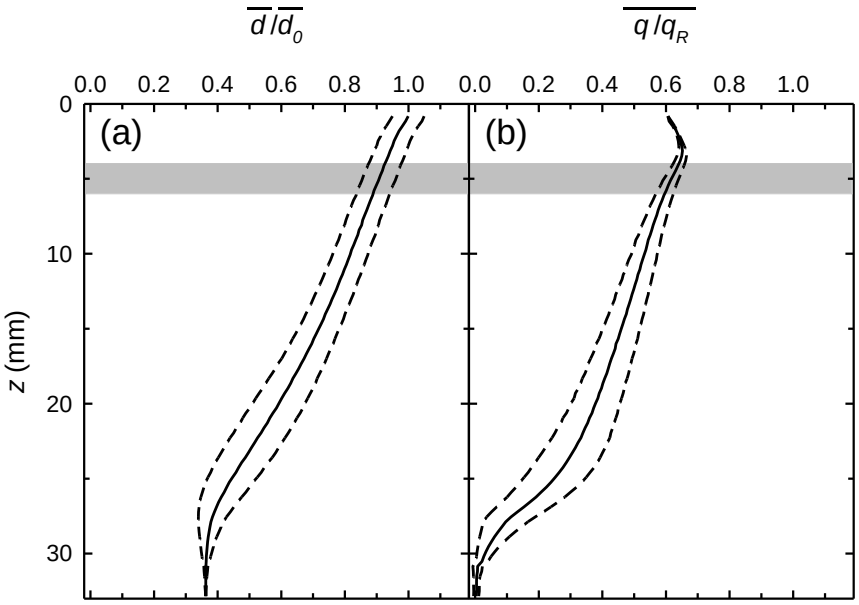

Fig. 10. Acetone droplets' averaged properties versus z for a system with upper-inlet gas speed $\overline{u_{g0}}$ of 4 m/s and ring height of 2 mm. The gray ribbon shows the position of the ring in z. a) Average droplet diameter normalized by the initial average diameter. b) Average of the droplet's charge to Rayleigh limit ratio. The dashed lines correspond to the average plus and minus one standard deviation.

Fig. 9 shows the ionic and droplets' electric currents versus z. The flyback trajectories have a zero net contribution to the current. Between the plate and the ring ($33 > z > 6$ mm), the ionic and droplets' current traces mirror each other, such that the total current ($I_d + I_{ion}$) remains constant, as charge is exchanged when the ions are captured by the droplets. At the ring ($6 > z > 4$ mm), the total current sharply drops mainly due to ion deposition onto the ring, while a small part of the ions' charge is transferred to the droplets. The ion current reaching the TC is negligible, posing no thread to its stability.

Fig. 10 shows the z-variation of the averaged droplet diameter normalized by its initial average value, $\bar{d}/\overline{d_0}$, and of the averaged charge-to-Rayleigh-charge ratio, $\overline{q/q_R}$. The Rayleigh charge q_R is the droplet's *own* Rayleigh limit charge, $(8\pi^2\varepsilon_0\sigma d^3)^{1/2}$ (see Eq. 8), computed individually for each droplet before averaging. Continuous lines are used for the average, and dotted lines for the average plus and minus one standard deviation. Panel (a) shows the progressive decline of the average droplet diameter while the droplets evaporate as they travel through the system, until the solid residue size of 2.9 μm (Table 1) is attained toward the bottom of the system ($z \gtrsim 28$ mm). Panel (b) shows that the charge-to-Rayleigh-limit ratio increases slightly, immediately after the droplets are introduced in the system. This happens as the

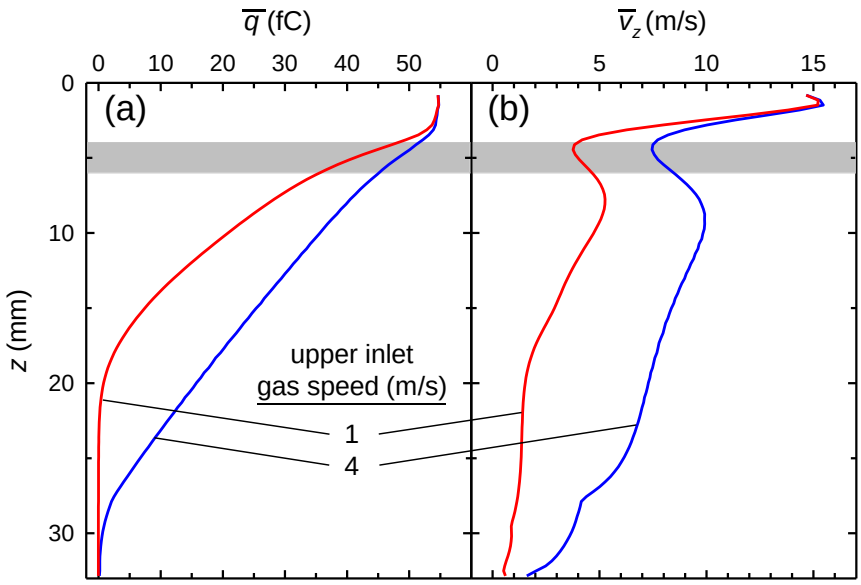

Fig. 11. Axial profiles of the average droplet charge (a) and z-component of the droplets' velocity (b) for an acetone spray with 2 mm ring height and two gas speeds $\overline{u_{g0}}$ of 1 and 4 m/s. The gray ribbon shows the position of the ring in z. Below z = 4 mm, the differences in droplet velocities are often well above the differences in incoming gas velocity ($\Delta\overline{u_{g0}}$ = 3 m/s). The additional increase in droplet axial speed can be attributed to the electrophoretic component (see text), which is larger on the droplets for the 4 m/s case, compared to the 1 m/s case, due to the large charge differences shown in panel (a).

droplets evaporate at constant charge, as very few ions combine with droplets in this region. Meanwhile, the standard deviation also increases from its initial zero value. If the droplets did not capture any ions at any z, the two tendencies (of growing average and standard deviation) would continue with until CFs would arise (even before the "upper" standard-deviation line would reach one; as shown in Appendix A). However, as the droplets start capturing ions, the charge ratio starts to decrease above the ring. This decrease happens even though the Rayleigh-limit charge q_R in the denominator also decreases. At z ~ 25 mm, the charge ratio decay is accelerated as the droplets start reaching the residue size and the denominator (q_R) becomes constant.

Fig. 11(a) shows the axial profiles of the average droplet charge $\bar{q}$ for two values of the upper-inlet air speed ($\overline{u_{g0}}$), 1 and 4 m/s. The droplets' charge loss is gradual but effective in both cases, with a very low value of the final droplet charge (of negative polarity). At any z, droplets in faster air move faster; therefore, have had less time for discharge by ion capture. This difference in available time for discharge leads to the different droplet charge shown. Note that the discharging kinetics is influenced by ion concentration, and that this concentration is

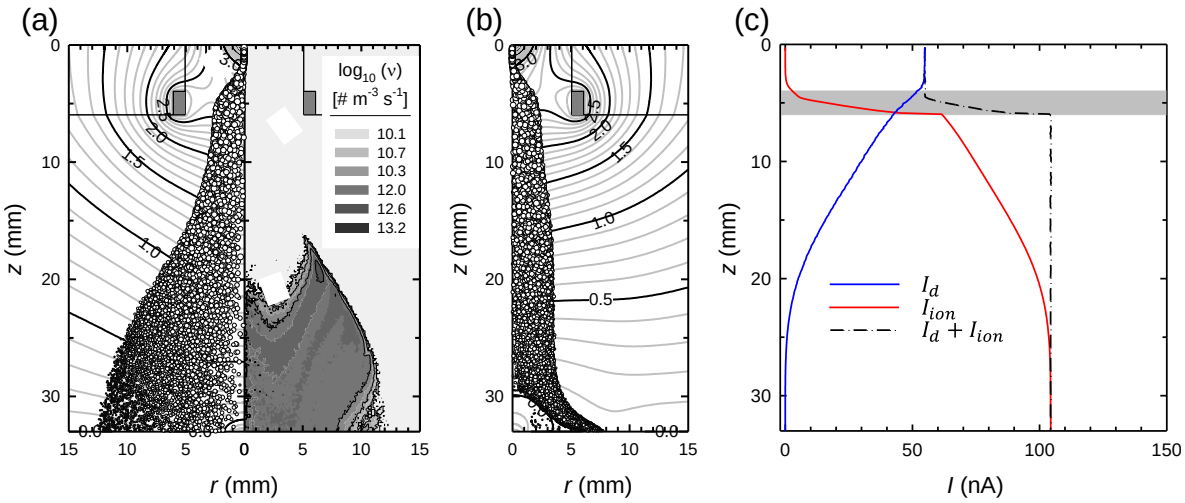

Fig. 12. Snapshots, equipotential lines (in kV) and density of Coulomb fissions rate for an electrospray of methanol when the upper-inlet gas speed $\overline{u_{g0}}$ is 2 m/s and the ring height is 2 mm. a) Case without ions: snapshot and equipotential lines for droplets (left) and density of Coulomb fissions rate (right). b) Case with ions: Snapshot and equipotential lines (where there are no Coulomb fission events). c) Axial dependence of the electric currents. The gray ribbon shows the position of the ring in z. The blue line indicates the current due to the droplets, the red line is the current due to the ions, and the black-dashed and dotted line is the overall current (sum of the currents due to droplets and ions).

distributed similarly in both of the simulations. This is primarily due to the fact that the dynamics of the ions are predominantly governed by electrostatic forces, and are minimally affected by the speed of the gas.

Fig. 11(b) shows the axial profiles of the average z-component of the droplet velocity vector. Initially, all the droplets are introduced at the jet speed. After a short electrostatic acceleration, their speed decreases due to the weakening electric field. Just above the ring (z = 4 mm) where the electric field is relatively weak (Fig. 7), the droplets are strongly governed by the gas velocity field. Therefore, in that zone, the droplets' speeds for the two traces differs by about the gas velocity difference of 3 m/s. Beyond z = 4 mm, the speed difference grows significantly beyond 3 m/s. This can be attributed to variations in the electrophoretic contribution ($K_d E$) to the droplets' velocity, which arise from differences in the electric mobilities of the droplets. The slower-moving droplets (red line) exhibit a faster decline in K_d because at any given z, they have lost a greater amount of charge due to their more prolonged ion capture (as Fig. 11(a) shows). This effect persists despite the counteractive contribution to electrical mobility caused by the reduction in droplet size by evaporation.

4.4 Effects of solvent volatility (with ions)

We next compare the behaviors of acetone and methanol sprays. We consider methanol in simulations with and without ions for a 2 mm ring height and gas speed of 2 m/s.

In the absence of ions, the spray plume for methanol, shown in Fig. 12(a), is wider than for acetone shown earlier in Fig. 5(a). The electric current for methanol is a bit higher than for acetone (Table 1, footnote b). The corresponding larger droplet charge for methanol leads to greater electric repulsion forces, hence a plume that expands faster in its early stages, and therefore, remains wider downstream. Another difference between the two solvents' sprays is the location of the CFs, which is closer to the plate for methanol (Fig. 12 (a) versus Fig. 5). This is expected as the methanol droplets evaporate slower due to its lower vapor pressure. Therefore, the methanol droplets reach the Rayleigh limit later in their lifetimes, when the spray is more expanded and diluted. Consequently also, the CF rate density is lower than for acetone.

After adding ions to the system, the methanol spray becomes significantly thinner, as shown in the snapshot of Fig. 12 (b), similarly as for the case of acetone (Figs. 6 and 7). In addition, as for the case of acetone, adding ions causes the compression of the equipotential lines toward the ring, as the capture of ions by the droplets reduces the spray's space charge between the ring and the plate. Figure 12 (c) shows the electric currents due to the droplets and the ions, versus the axial coordinate (z). These functions show similar tendencies as for acetone for a faster air velocity of 4 m/s (Fig. 9), and the same velocity of 2 m/s (Appendix A). The similarity of the data between the two solvents confirms that the in-situ electrospray discharging by the proposed configuration adapts itself robustly to changes in solvent volatility.

Figure 13 compares some droplet properties versus z for electrosprays for the two solvents at equal ring height and upper-inlet gas speed. Panel (a) shows the trends of the average droplet diameter. As expected, the acetone droplets' diameter decreases more rapidly with z, levelling off as the droplets reach the residue value of 2.9 µm. The methanol droplets' diameter does not level off within the simulation domain. For acetone, the droplet size decay is steeper than as shown earlier for $\overline{u_{g0}}$ = 4 m/s in Fig. 10(a). There are two reasons for this, mainly. On the one hand, faster air helps to carry the droplets downstream faster by convective transport. Hence, at the same z we expect to find younger, thus less evaporated, larger droplets. On the other hand, the younger droplets had less time to collect ions; therefore, they hold more charge, thus having higher electric mobility despite being larger.

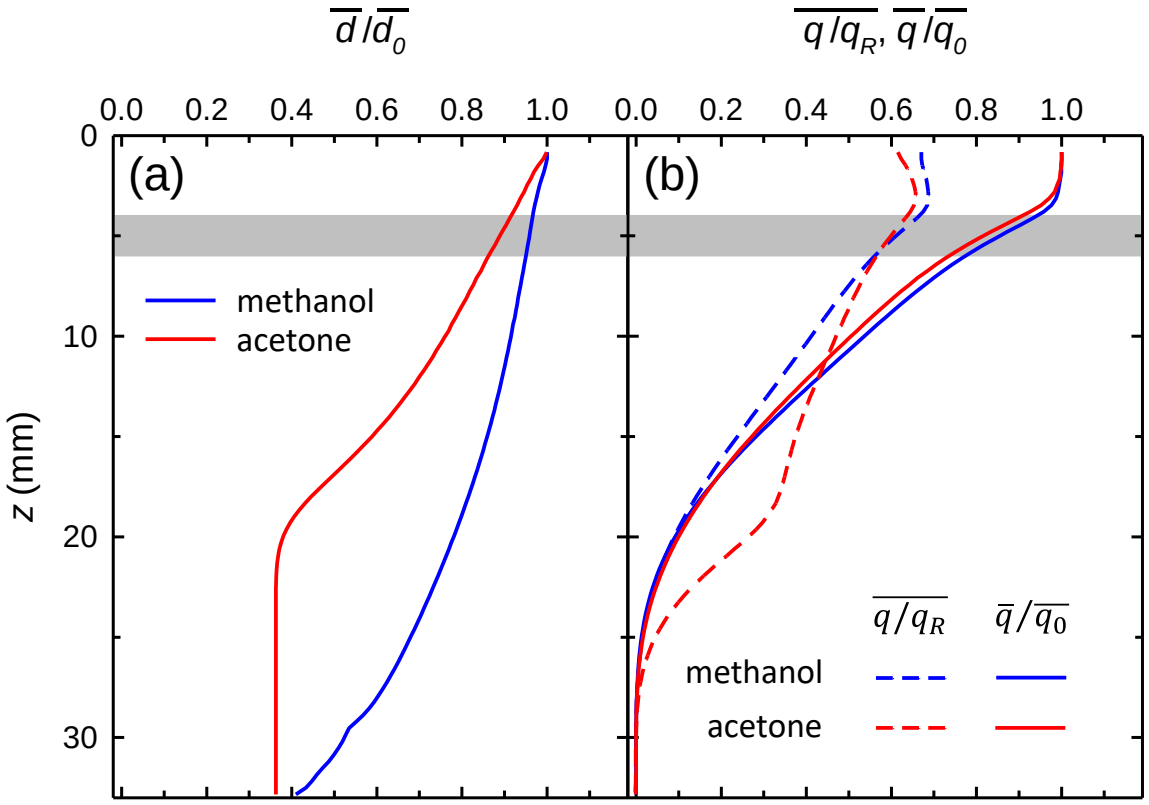

Fig. 13. Acetone and methanol droplets' characteristics averaged across r along z. Upper-inlet gas speed $\overline{u_{g0}}$ is 2 m/s and ring height l_R is 2 mm. a) Average droplet diameter over the average initial droplet diameter. b) Average droplet charge over either the average initial charge or the individual Rayleigh limit charge. The red lines correspond to acetone, whereas the blue lines to methanol. The gray ribbon shows the position of the ring in z.

Panel (b) of Fig. 13 shows for the two solvents the z profiles of two variables related to the droplet charge. One is $\overline{q/q_R}$, the radially averaged ratio of the droplets' charge to their own Rayleigh limit charge, and the other is $\bar{q}/\overline{q_0}$, the radially averaged droplets' charge normalized by the initial average charge value ("normalized charge").

Regarding the latter, the two $\bar{q}/\overline{q_0}$ profiles are very similar. This may seem surprising at first, since the droplet size profiles of panel (a) are so different. Yet, the discharge rate of a droplet is independent of the droplet's diameter for most of the discharging process, where $dq/dt = K_I \rho_{ion} E/\varepsilon_0$, which only depends on the ions' electric mobility and concentration, and the electric field strength (Pauthenier and Moreau-Hanot, 1932). Therefore, the discharging profiles (average charge versus z) may be similar so long as the droplet speeds are similar, and the droplets are exposed to approximately the same ion concentrations and electric fields, as is

the case. Furthermore, normalizing by the initial charge (which was different for acetone and methanol; Table 1) helps reduce the differences between the two $\bar{q}/\overline{q_0}$ profiles even more.

Regarding $\overline{q/q_R}$ in Fig. 13 (b), it is dependent on two competing processes: the droplet evaporation dynamics (lowering the denominator, i.e., the Rayleigh charge) and the discharge dynamics by ion capture (lowering the numerator, i.e., the droplet's charge). Droplets of acetone and methanol have very similar charge at a given z, as established by the $\bar{q}/\overline{q_0}$ traces. On the other hand, the denominator (q_R) decreases slower for methanol than for acetone, as the methanol droplets evaporate slower. This causes the charge ratio $\overline{q/q_R}$ to decrease faster for methanol than for acetone.

5. Conclusions

Solid particles of small, uniform size can be produced by the drying of electrospray droplets containing a non-volatile component. The electric charge is the key element allowing to attain tiny droplet sizes by electrospray. However, after the droplets are formed their charge causes them to drift very rapidly towards the counter electrode, where they can be collected wet. In addition, Coulomb fissions often occur which result in a dispersion of the particle size and in irregular, undesirable particle shapes. In this study we have investigated the process of in-situ droplet discharging by means of corona ions, with the aim to avoid these problems.

We have developed a mathematical model and conducted numerical simulations to investigate this problem. The model includes Lagrangian tracking of the droplets, their evaporation, their Coulomb fission, the Eulerian description of the ions' and progeny droplets' transports, and the droplet discharge kinetics by ion capture.

We have analyzed which geometrical and process factors are more suitable to completely prevent droplet Coulomb fissions, while avoiding any significant ion transfer to the Taylor cone, and to efficiently extract the discharged droplets/particles from the system. A suitable configuration comprises a capillary that supports a Taylor cone, wherefrom electrospray droplets are emitted, and a plate, acting as counter electrode. The plate contains a central orifice wherefrom the ions are emitted with an electric current that is somewhat higher than the current of the electrospray droplets. In the model, the emission of ions is obtained by a realistic simulation of a corona discharge located behind the orifice. On exiting the orifice, the ionic

cloud expands rapidly, driven by the strong electrostatic repulsion between the ions. About a fourth of these ions is distributed across the entire width of the droplet plume, while the rest of the ions return back to the plate. Additionally, a gas stream flows through the system in the same direction as the droplets to drag the discharged droplets out of the system, exiting through a circular slot in the plate.

In addition, a conductive ring is placed around the capillary to collect the excess ions (ions not captured by drops) while protecting the Taylor cone from the ions. This protection is achieved by selecting the geometry and potential of the ring to sufficiently weaken the electric field, thereby preventing ions from reaching the Taylor cone. Simultaneously, the resulting electric field ensures that the droplets are not directed towards the ring, thus avoiding their deposition on the ring's surface. In addition, the gas is forced through the ring's opening, where it helps push the droplets through the region where the electric field is weak.

We have simulated two electrospray systems with identical droplet size distributions but different volatilities of the solvents (acetone and methanol). In these systems, most of the droplets lose charge downstream of the ring, before they undergo the first Coulomb fission. Importantly, when the ring is thin and short, it attracts the majority of excess ions. The remaining ions pass through the ring towards the Taylor cone, but are intercepted by the spray, thus preventing the ions from reaching the Taylor cone and trigger instability.

In conclusion, our simulations demonstrate that the axial configuration comprising a ring and an orifice plate placed between the spraying and corona tips is an excellent strategy to obtain stable and efficient in-situ discharging and extraction of electrospray plumes.

Funding

This study was funded by the Spanish Government through grants PGC2018-099687-B-I00 (MCI/AEI/FEDER, UE) and DPI2015-68969-P (MINECO/FEDER, UE), and by the Catalan Government through grants 2017SGR1516 and 2021SGR-00978 (AGAUR).

Declaration of competing interest

The authors declare that they have no known competing financial interests or personal relationships that could have appeared to influence the work reported in this paper.

Data availability

Data will be made available on request.

Acknowledgements

This project has been carried out using computational resources of the *Consorci de Serveis Universitaris de Catalunya* (CSUC).

Appendix A. Supplementary data

Supplementary data to this article can be found online at XXX

References

Abraham, F. F. (1970). Functional Dependence of Drag Coefficient of a Sphere on Reynolds Number. *Physics of Fluids*, *13*(8), 2194. https://doi.org/10.1063/1.1693218

Adamiak, K., & Atten, P. (2004). Simulation of corona discharge in point-plane configuration. *Journal of Electrostatics*, *61*(2), 85–98. https://doi.org/10.1016/j.elstat.2004.01.021

Adamiak, K., Atrazhev, V., & Atten, P. (2005). Corona discharge in the hyperbolic point-plane configuration: Direct ionization criterion versus approximate formulations. *IEEE Transactions on Dielectrics and Electrical Insulation*, *12*(5), 1025–1033. https://doi.org/10.1109/TDEI.2005.1522195

Allen, M. D., & Raabe, O. G. (1982). Re-evaluation of Millikan's oil drop data for the motion of small particles in air. *Journal of Aerosol Science*, *13*(6), 537–547. https://doi.org/10.1016/0021-8502(82)90019-2

Almería, B., & Gomez, A. (2014). Electrospray synthesis of monodisperse polymer particles in a broad (60 nm-2 μm) diameter range: Guiding principles and formulation recipes.

Journal of Colloid and Interface Science, *417*, 121–130. https://doi.org/10.1016/j.jcis.2013.11.037

Arumugham-Achari, A. K., Grifoll, J., & Rosell-Llompart, J. (2013). Two-way coupled numerical simulation of electrospray with induced gas flow. *Journal of Aerosol Science*, *65*, 121–133. https://doi.org/10.1016/j.jaerosci.2013.07.005

Arumugham-Achari, A.K., Grifoll, J., Rosell-Llompart, J. (2015). A comprehensive framework for the numerical simulation of evaporating electrosprays. Aerosol Sci. Technol. 49, 436–448. https://doi.org/10.1080/02786826.2015.1039639

Benassayag, G., Sudraud, P., & Jouffrey, B. (1985). In situ high voltage tem observation of an electrohydrodynamic (EHD) ion source. *Ultramicroscopy*, *16*(1), 1–8. https://doi.org/10.1016/S0304-3991(85)80002-4

Bocanegra, R., Galán, D., Márquez, M., Loscertales, I. G., & Barrero, A. (2005). Multiple electrosprays emitted from an array of holes. *Journal of Aerosol Science*, *36*(12), 1387–1399. https://doi.org/10.1016/j.jaerosci.2005.04.003

Boda, S. K., Li, X., & Xie, J. (2018). Electrospraying an enabling technology for pharmaceutical and biomedical applications: A review. *Journal of Aerosol Science*, *125*, 164–181. https://doi.org/10.1016/j.jaerosci.2018.04.002

Bodnár, E., & Rosell-Llompart, J. (2013). Growth dynamics of granular films produced by electrospray. *Journal of Colloid and Interface Science*, *407*, 536–545. https://doi.org/10.1016/j.jcis.2013.06.013

Bodnár, E., Grifoll, J., & Rosell-Llompart, J. (2018). Polymer solution electrospraying: A tool for engineering particles and films with controlled morphology. *Journal of Aerosol Science*, *125*, 93–118. https://doi.org/10.1016/j.jaerosci.2018.04.012

Borra, J.-P. (2018). Review on water electro-sprays and applications of charged drops with focus on the corona-assisted cone-jet mode for High Efficiency Air Filtration by wet electro-scrubbing of aerosols. *Journal of Aerosol Science*, *125*, 208–236. https://doi.org/10.1016/j.jaerosci.2018.04.005

Carrasco-Munoz, A., Barbero-Colmenar, E., Bodnár, E., Grifoll, J., & Rosell-Llompart, J. (2022). Monodisperse droplets and particles by efficient neutralization of electrosprays. *Journal of Aerosol Science*, *160*, 105909. https://doi.org/10.1016/j.jaerosci.2021.105909

Castillo, J. L., Martin, S., Rodriguez-Perez, D., Higuera, F. J., & Garcia-Ybarra, P. L. (2018). Nanostructured porous coatings via electrospray atomization and deposition of nanoparticle suspensions. *Journal of Aerosol Science*, *125*, 148–163. https://doi.org/10.1016/j.jaerosci.2018.03.004

Chen, D. R., Pui, D. Y. H., & Kaufman, S. L. (1995). Electrospraying of conducting liquids for monodisperse aerosol generation in the 4 nm to 1.8 μm diameter range. *Journal of Aerosol Science*, *26*(6), 963–977. https://doi.org/10.1016/0021-8502(95)00027-A

Ciach, T. (2006). Microencapsulation of drugs by electro-hydro-dynamic atomization. International *Journal of Pharmaceutics*, *324*(1), 51–55. https://doi.org/10.1016/j.ijpharm.2006.06.035

Cloupeau, M. (1994). Recipes for use of EHD spraying in cone-jet mode and notes on corona discharge effects. *Journal of Aerosol Science*, *25*(6), 1143–1157. https://doi.org/10.1016/0021-8502(94)90206-2

COMSOL Multiphysics version 5.2a. (2016) https://www.comsol.com/.

de Juan, L., & Fernández de la Mora, J. (1997). Charge and size distributions of electrospray drops. *Journal of Colloid and Interface Science*, *186*, 280–293. https://doi.org/10.1006/jcis.1996.4654

Deng, W., & Gomez, A. (2007). Influence of space charge on the scale-up of multiplexed electrosprays. *Journal of Aerosol Science*, *38*(10), 1062–1078. https://doi.org/10.1016/j.jaerosci.2007.08.005

Ermak, D. L., & Buckholz, H. (1980). Numerical integration of the Langevin equation: Monte Carlo simulation. *Journal of Computational Physics*, *35*(2), 169–182. https://doi.org/10.1016/0021-9991(80)90084-4

Fenn, J. B. (2003). Electrospray wings for molecular elephants (Nobel lecture). *Angewandte Chemie International Edition*, *42*(33), 3871–3894. https://doi.org/10.1002/anie.200300605

Fernández de la Mora, J. (1992). The effect of charge emission from electrified liquid cones. *Journal of Fluid Mechanics*, *243*, 561–574. https://doi.org/10.1017/S0022112092002829

Fletcher, C. A. J. (2005). Computational Techniques for Fluid Dynamics 1. In *Computational Techniques for Fluid Dynamics 1* (2nd ed.). Springer Berlin Heidelberg. https://doi.org/10.1007/978-3-642-58229-5

Gamero-Castaño, M., & Hruby, V. (2001). Electrospray as a source of nanoparticles for efficient colloid thrusters. *Journal of Propulsion and Power*, *17*(5), 977–987. https://doi.org/10.2514/2.5858

Gañán-Calvo, A. M., Dávila, J., & Barrero, A. (1997). Current and droplet size in the electrospraying of liquids. Scaling laws. *Journal of Aerosol Science*, *28*(2), 249–275. https://doi.org/10.1016/S0021-8502(96)00433-8

Gomez, A., & Tang, K. (1991). Characterization of a high charge density electrospray of methanol. *Fifth International Conference on Liquid Atomization and Spray Systems, ICLASS-91*.

Gomez, A., & Tang, K. (1994). Charge and fission of droplets in electrostatic sprays. *Physics of Fluids*, *6*(1), 404–414. https://doi.org/10.1063/1.868037

Grifoll, J., & Rosell-Llompart, J. (2012). Efficient Lagrangian simulation of electrospray droplets dynamics. *Journal of Aerosol Science*, *47*, 78–93. https://doi.org/10.1016/j.jaerosci.2012.01.001

Grifoll, J., & Rosell-Llompart, J. (2014). Continuous droplets' charge method for the Lagrangian simulation of electrostatic sprays. *Journal of Electrostatics*, *72*(5), 357–364. https://doi.org/10.1016/j.elstat.2014.06.011

Grimm, R. L., & Beauchamp, J. L. (2002). Evaporation and discharge dynamics of highly charged droplets of heptane, octane, and p-xylene generated by electrospray ionization. *Analytical Chemistry*, *74*(24), 6291–6297. https://doi.org/10.1021/ac025889b

Grimm, R. L., & Beauchamp, J. L. (2005). Dynamics of field-induced droplet ionization: Time-resolved studies of distortion, jetting, and progeny formation from charged and neutral methanol droplets exposed to strong electric fields. *Journal of Physical Chemistry B*, *109*(16), 8244–8250. https://doi.org/10.1021/jp0450540

Grimm, R. L., & Beauchamp, J. L. (2010). Evaporation and discharge dynamics of highly charged multicomponent droplets generated by electrospray ionization. *Journal of Physical Chemistry A*, *114*(3), 1411–1419. https://doi.org/10.1021/jp907162w

Hartman, R. P. A., Brunner, D. J., Camelot, D. M. A., Marijnissen, J. C. M., & Scarlett, B. (2000). Jet break-up in electrohydrodynamic atomization in the cone-jet mode. *Journal of Aerosol Science*, *31*(1), 65–95. https://doi.org/10.1016/S0021-8502(99)00034-8

Higuera, F. J. (2012). Eulerian model of a dilute spray of charged droplets. *Journal of Aerosol Science*, *48*, 34–45. https://doi.org/10.1016/j.jaerosci.2012.01.008

Higuera, F. J. (2016). Neutralization of a spray of electrically charged droplets by a corona discharge. *Journal of Fluid Mechanics*, 801, 130–149. https://doi.org/10.1017/jfm.2016.449

Hinds, W. C. (1999). *Aerosol technology: properties, behavior, and measurement of airborne particles*. Wiley.

Hunter, H. C., & Ray, A. K. (2009). On progeny droplets emitted during Coulombic fission of charged microdrops. *Physical Chemistry Chemical Physics: PCCP*, *11*(29), 6156–6165. https://doi.org/10.1039/b820457h

Ijsebaert, J. C., Geerse, K. B., Marijnissen, J. C. M., Lammers, J. W., & Zanen, P. (2001). Electro-hydrodynamic atomization of drug solutions for inhalation purposes. *Journal of Applied Physiology*, *91*(6), 2735–2741. https://doi.org/10.1152/jappl.2001.91.6.2735

Ismail, A. S., Yao, J., Xia, H. H., & Stark, J. P. W. (2018). Breakup length of electrified liquid jets: Scaling laws and applications. *Physical Review Applied*, *10*(6), 64010. https://doi.org/10.1103/PhysRevApplied.10.064010

Jaworek, A., Sobczyk, A. T., & Krupa, A. (2018). Electrospray application to powder production and surface coating. *Journal of Aerosol Science*, *125*, 57–92. https://doi.org/10.1016/j.jaerosci.2018.04.006

Kavadiya, S., & Biswas, P. (2018). Electrospray deposition of biomolecules: Applications, challenges, and recommendations. *Journal of Aerosol Science*, *125*, 182–207. https://doi.org/10.1016/j.jaerosci.2018.04.009

Kelder, E. M., Marijnissen, J. C. M., & Karuga, S. W. (2018). EDHA for energy production, storage and conversion devices. *Journal of Aerosol Science*, *125*, 119–147. https://doi.org/10.1016/j.jaerosci.2018.04.011

Khalifehei, M., & Higuera, F. J. (2020). Neutralization of an electrospray by a corona discharge. *Journal of Aerosol Science*, 145, 105547. https://doi.org/10.1016/j.jaerosci.2020.105547

Khalifehei, M., & Higuera, F. J. (2023). One dimensional model of electrospray neutralization. *Journal of Aerosol Science*, *170*(February), 106145. https://doi.org/10.1016/j.jaerosci.2023.106145

Larriba-Andaluz, C., & Fernández de la Mora, J. (2010). Electrospraying insulating liquids via charged nanodrop injection from the Taylor cone of an ionic liquid. *Physics of Fluids*, *22*(7), 1–7. https://doi.org/10.1063/1.3455992

Lawless, P. A. (1996). Particle charging bounds, symmetry relations, and an analytic charging rate model for the continuum regime. *Journal of Aerosol Science*, *27*(2), 191–215. https://doi.org/10.1016/0021-8502(95)00541-2

Li, K. Y., Tu, H., & Ray, A. K. (2005). Charge limits on droplets during evaporation. *Langmuir*, *21*(9), 3786–3794. https://doi.org/10.1021/la047973n

López Urdiales, J. M. (2004). *Progress in colloid propulsion* [Massachusetts Institute of Technology]. http://hdl.handle.net/1721.1/28891

Lord Rayleigh F.R.S. (1882). On the equilibrium of liquid conducting masses charged with electricity. *The London, Edinburgh, and Dublin Philosophical Magazine and Journal of Science*, *14*(87), 184–186. https://doi.org/10.1080/14786448208628425

Meesters, G. M. H., Vercoulen, P. H. W., Marijnissen, J. C. M., & Scarlett, B. (1992). Generation of micron-sized droplets from the Taylor cone. *Journal of Aerosol Science*, *23*(1), 37–49. https://doi.org/10.1016/0021-8502(92)90316-N

Miller, R. S., Harstad, K., & Bellan, J. (1998). Evaluation of equilibrium and non-equilibrium evaporation for many-droplet gas-liquid flow simulations. *International Journal of Multiphase Flow*, *24*(6), 1025–1055. https://doi.org/10.1016/S0301-9322(98)00028-7

Montanero, J. M., & Gañán-Calvo, A. M. (2020). Dripping, jetting and tip streaming. *Reports on Progress in Physics*, *83*(9), 97001. https://doi.org/10.1088/1361-6633/aba482

Mustika, W. S., Hapidin, D. A., Saputra, C., & Munir, M. M. (2021). Dual needle corona discharge to generate stable bipolar ion for neutralizing electrosprayed nanoparticles. *Advanced Powder Technology*, *32*(1), 166–174. https://doi.org/10.1016/j.apt.2020.11.026

Noakes, T. J., Pavey, I. D., Bray, D., & Rowe, R. C. (1989). Apparatus for Producing a Spray of Droplets of a Liquid (Patent No. US Patent 4,829,996). USPTO. https://pdfpiw.uspto.gov/.piw?PageNum=0&docid=04829996

Pantano, C., Gañán-Calvo, A. M., & Barrero, A. (1994). Zeroth-order, electrohydrostatic solution for electrospraying in cone-jet mode. *Journal of Aerosol Science*, *25*(6), 1065–1077. http://dx.doi.org/10.1016/0021-8502(94)90202-X

Pauthenier, M., & Moreau-Hanot, M. (1932). La charge des particules sphériques dans un champ ionisé. *Journal de Physique et Le Radium*, *3*(12), 590–613. https://doi.org/10.1051/jphysrad:01932003012059000

Pillai, R., Berry, J. D., Harvie, D. J. E., & Davidson, M. R. (2016). Electrokinetics of isolated electrified drops. *Soft Matter*, *12*(14), 3310–3325. https://doi.org/10.1039/c6sm00047a

Qu, J., Zeng, M., Zhang, D., Yang, D., Wu, X., Ren, Q., & Zhang, J. (2021). A review on recent advances and challenges of ionic wind produced by corona discharges with practical applications. *Journal of Physics D: Applied Physics*, *55*(15), 153002. https://doi.org/10.1088/1361-6463/ac3e2c

Rosell-Llompart, J., Grifoll, J., & Loscertales, I. G. (2018). Electrosprays in the cone-jet mode: From Taylor cone formation to spray development. *Journal of Aerosol Science*, *125*, 2–31. https://doi.org/10.1016/j.jaerosci.2018.04.008

Rulison, A. J., & Flagan, R. C. (1994). Synthesis of yttria powders by electrospray pyrolysis. *Journal of the American Ceramic Society*, *77*(12), 3244–3250. https://doi.org/10.1111/j.1151-2916.1994.tb04577.x

Saville, D. A. (1997). Electrohydrodynamics: The Taylor-Melcher leaky dielectric model. *Annual Review of Fluid Mechanics*, *29*(1), 27–64. https://doi.org/10.1146/annurev.fluid.29.1.27

Sazhin, S. S. (2017). Modelling of fuel droplet heating and evaporation: Recent results and unsolved problems. *Fuel*, *196*, 69–101. https://doi.org/10.1016/j.fuel.2017.01.048

Seinfeld, J. H., & Pandis, S. N. (2016). *Atmospheric Chemistry and Physics* (Third edit). John Wiley & Sons, Inc.

Singh, M., Gawande, N., Mayya, Y. S., & Thaokar, R. (2019). Effect of the Quadrupolar Trap Potential on the Rayleigh Instability and Breakup of a Levitated Charged Droplet. *Langmuir*, *35*(48), 15759–15768. https://doi.org/10.1021/acs.langmuir.9b02547

Smith, D. P. H. (1986). The electrohydrodynamic atomization of liquids. *IEEE Transactions on Industry Applications*, *IA-22*(3), 527–535. https://doi.org/10.1109/TIA.1986.4504754

Sochorakis, N., Grifoll, J., & Rosell-Llompart, J. (2019). Scaling up of extractor-free electrosprays in linear arrays. *Chemical Engineering Science*, *195*, 281–298. https://doi.org/10.1016/j.ces.2018.09.006

Tang, K., & Gomez, A. (1994b). Generation by electrospray of monodisperse water droplets for targeted drug delivery by inhalation. *Journal of Aerosol Science*, *25*(6), 1237–1249. https://doi.org/10.1016/0021-8502(94)90212-7

Tang, J., Wang, H., & Gomez, A. (2017). Controlled nanoparticle synthesis via opposite-polarity electrospray pyrolysis. *Journal of Aerosol Science*, *113*, 201–211. https://doi.org/10.1016/j.jaerosci.2017.07.001

Taylor, G. (1964). Disintegration of water drops in an electric field. *Proceedings of the Royal Society A: Mathematical, Physical and Engineering Sciences*, *280*(1382), 383–397. https://doi.org/10.1098/rspa.1964.0151

Vu, T., Yadav, S., Tran, C., Nguyen, H.-Q., Nguyen, T.-H., Nguyen, T., Nguyen, T.-K., Fastier-Wooller, J. W., Dinh, T., Phan, H., Ta, H. T., Nguyen, N., Dao, D. V., & Dau, V. T. (2023). Charge-Reduced Particles via Self-Propelled Electrohydrodynamic Atomization for Drug Delivery Applications. *ACS Applied Materials & Interfaces*. https://doi.org/10.1021/acsami.3c02000

Xie, J., Marijnissen, J. C. M., & Wang, C. H. (2006). Microparticles developed by electrohydrodynamic atomization for the local delivery of anticancer drug to treat C6 glioma in vitro. *Biomaterials*, *27*(17), 3321–3332. https://doi.org/10.1016/j.biomaterials.2006.01.034

Yurkstas, E. P., & Meisenzehl, C. J. (1964). Solid homogeneous aerosol production by electrical atomization. AEC research and development report UR-652. Retrieved from https://pubmed.ncbi.nlm.nih.gov/14242770/

Zhang, J., Adamiak, K., & Castle, G. S. P. (2007). Numerical modeling of negative-corona discharge in oxygen under different pressures. *Journal of Electrostatics*, *65*(3), 174–181. https://doi.org/10.1016/j.elstat.2006.07.013

Zimlich, W., Ding, J., Busick, D., Pham, S., Palmer, D., & Placke, M. (2002). Development of multiple clinical and commercial applications using mystic inhalation delivery

technologies. In R. Dalby, P. Byron, J. Peart, & S. Farr (Eds.), *Respiratory Drug Delivery VIII* (pp. 363–366). RDD Online. https://www.rddonline.com/publications/proceedings/index.php

Appendix A

SUPPLEMENTARY INFORMATION

for article

In-situ charge reduction of electrospray plumes by unipolar corona ions

Jordi Grifoll[1] and Joan Rosell-Llompart[1,2]

[1] Department of Chemical Engineering, Universitat Rovira i Virgili, 43007 Tarragona, Spain.

[2] Catalan Institution for Research and Advanced Studies - ICREA, 08010 Barcelona, Spain.

S1. Simulation of the corona discharge

The electrospray simulations presented in the article required realistic boundary conditions for the flux of ions entering the electrospray chamber through the orifice from the corona chamber, as well as for the electric potential at the plate orifice (given in section S3 of this Appendix). These conditions were obtained by a full corona discharge simulation, based on the mathematical framework proposed by of Adamiak and Atten (2004) and Adamiak et al. (2005), as explained in the main text. This corona simulation procedure was compared to a common point-plane configuration test case presented by Adamiak and Atten (2004). In their study, they measured the experimental current generated by a corona discharge between a needle and a flat plate. Their needle's tip had an average radius of curvature of 95 μm and was positioned 3.1 cm above the grounded plate. With the needle set at a voltage of 8.0 kV they recorded a current of 2.47 μA, close to their simulation results. For the same electrode arrangement, our simulations based on their numerical procedure yield a current of 2.81 μA, which is reasonably close to their value and reassures us in the validity of using the procedure. The use of this approach in our full corona discharge simulation captures the complex interplay between the electric field, ion generation, and gas flow within the corona discharge chamber, leading to a more precise and reliable characterization of the electrospray behavior, including its discharging. The following figures show results from this simulation.

The simulation domain considers the corona chamber shown in Fig. SI-1, with the indicated boundary conditions for the electrical potential ϕ. For the top boundary, a realistic boundary condition which would be suitable for the electrospray simulations had to be developed. It was

obtained by an iterative procedure involving corona discharge and electrospray simulations (allowing for droplet discharging) for the representative case of acetone with $\overline{u_{g0}}$ = 4 m/s and l_R= 2 mm. For each of these electrospray simulations, the boundary conditions at the orifice exit plane were taken from the preceding corona discharge simulation, while for the subsequent corona discharge simulation, the electric potential at 6.2 mm above the plate was taken from the preceding electrospray simulation. The ion dynamics in the corona chamber and through the orifice is dominated by ionic space charge and is nearly uncoupled to the electrospray charge distribution. Therefore, to reduce the number of iterations needed, the distance of 6.2 mm was chosen (more than two orifice diameters above the orifice exit) in a region where the ion density is expected to be greatly diminished from the value at the orifice (as confirmed by the simulations, as shown in Fig. 8 of the main text). With this choice, the solutions converged after just two iterations. Because of the weak coupling between the electrospray and the corona dynamics (including the ion motion at the orifice), we considered the corona solution to be valid till the orifice exit plane, for all of the electrospray simulations presented in the article.

The ionic charge density (shown in Fig. SI-2) and the ion trajectories (Fig. SI-5) help appreciate that most of the generated ions are not transferred to the electrospray domain, but are collected on the plate's lower side and orifice wall. They also show that the ion cloud above the orifice suffers a rapid radial expansion, which is caused by the high space charge in that zone. As discussed in the article, the implication of this phenomenon is very significant for the subsequent simulations with electrosprays, because it allows the ions to cover the entire width of the electrospray plume thus promoting the discharge of droplets.

The gas velocity within the corona discharge chamber, shown in Fig. SI-4, has a negligible influence over the transport (trajectories) of the ions, due to the dominance of the electric force over the drag force on the ion. Nevertheless, the simulation of a velocity field, with an average velocity through the orifice of 1 m/s, was incorporated in the simulation of the ions' transport. This velocity profile has a local effect on the gas velocity field in the electrospray domain, in the electrospray simulations.

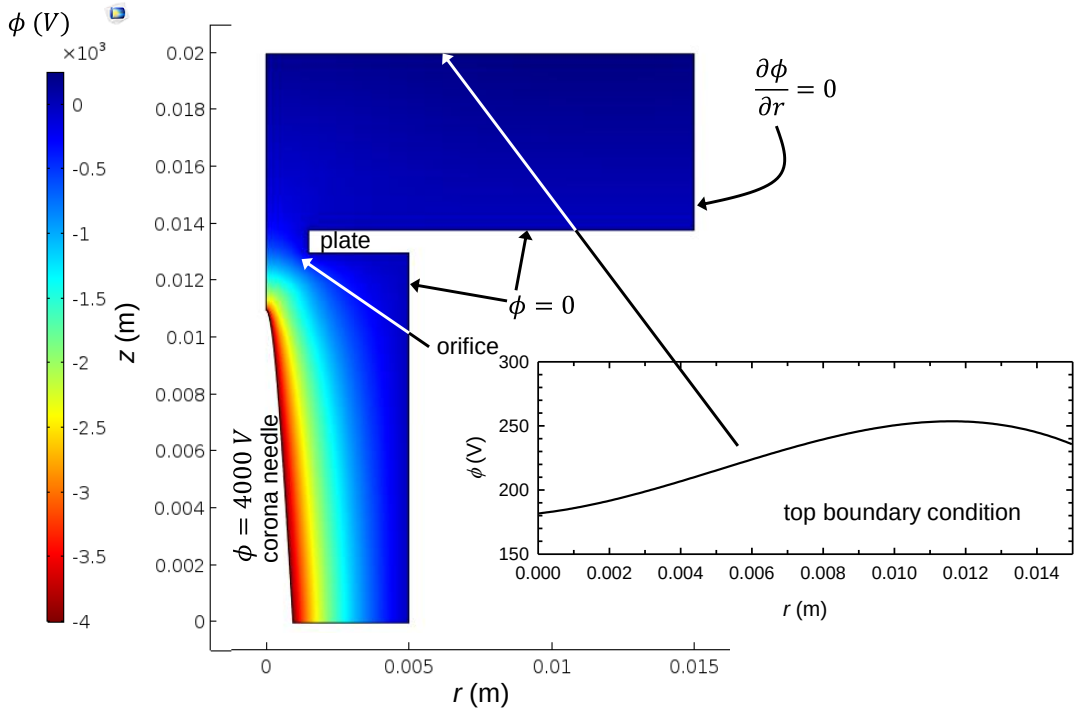

Fig. SI-1. Corona-simulation system domain and electric potential solution $\phi(r, z)$. The surface of the needle was set to 4000 V, while the walls of the corona chamber and the plate were Earth-grounded. The top boundary of the region above the plate was set at a potential given by the function $\phi = 181.7 + 3110 \cdot r + 1065416 \cdot r^2 - 68918524 \cdot r^3$, which was obtained by fitting the potential along r at 6.2 mm above the plate for the simulation of the electrospray dynamics (case: acetone with $\overline{u_{g0}}$ = 4 m/s and l_R= 2 mm). The needle shape is given by the following parametric equations for $r < 1$ mm: $r = 4.743 \times 10^{-4} \sinh(\xi)$ [in m]; $z = 9.000 \times 10^{-3} \cosh(\xi)$ [in m]. For larger z, $r = 1$ mm.

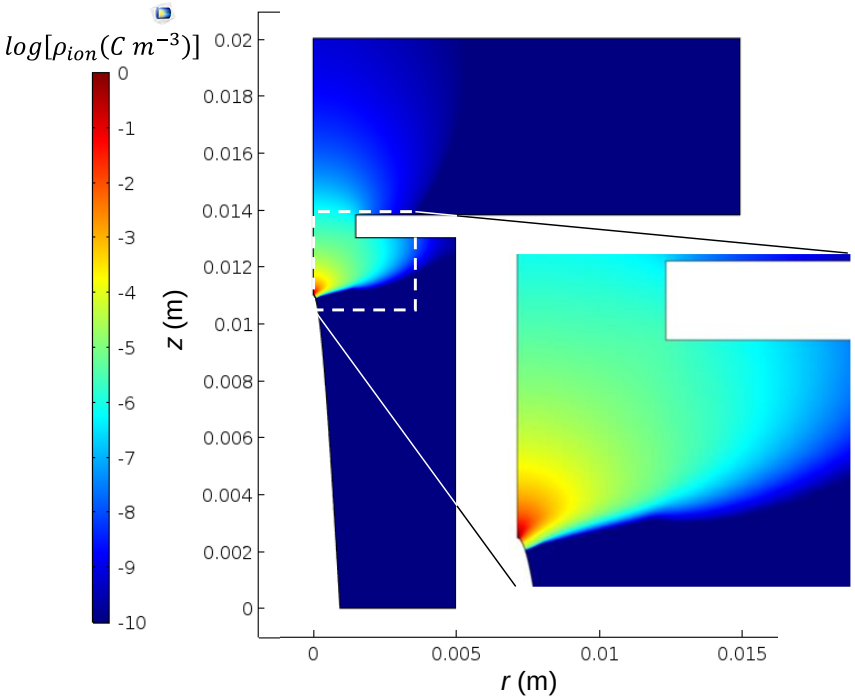

Fig. SI-2. Natural logarithm of the ion charge density. The density is highest in the corona chamber domain, below the orifice. After going through the orifice, the ions suffer a rapid radial expansion, which is caused by the high space charge they hold in that zone.

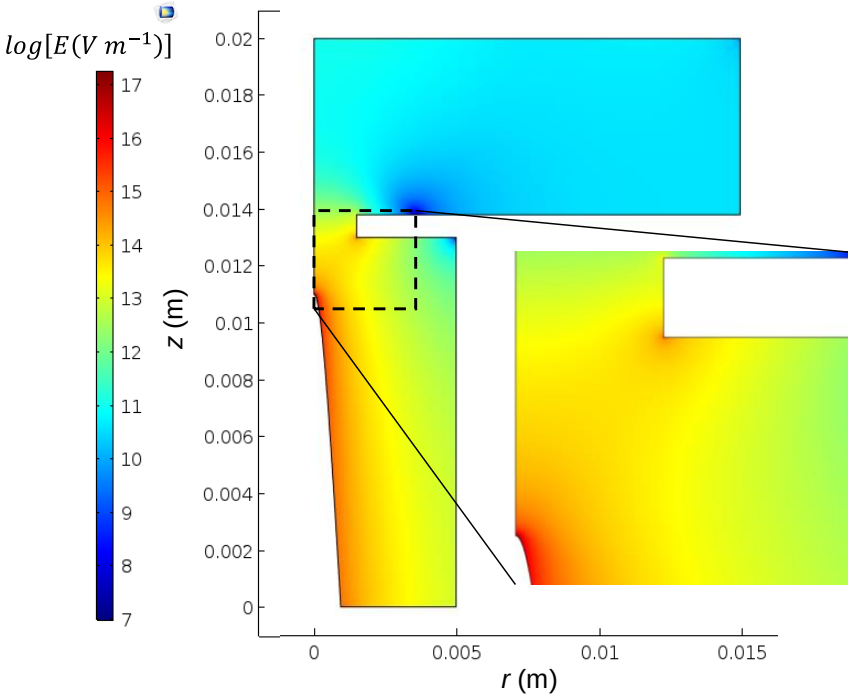

Fig. SI-3. Natural logarithm of the electric field modulus (field strength). The electric field is most intense inside the corona chamber, as expected. On the electrospray side, minimum of the electric field modulus is located on the plate near the orifice.

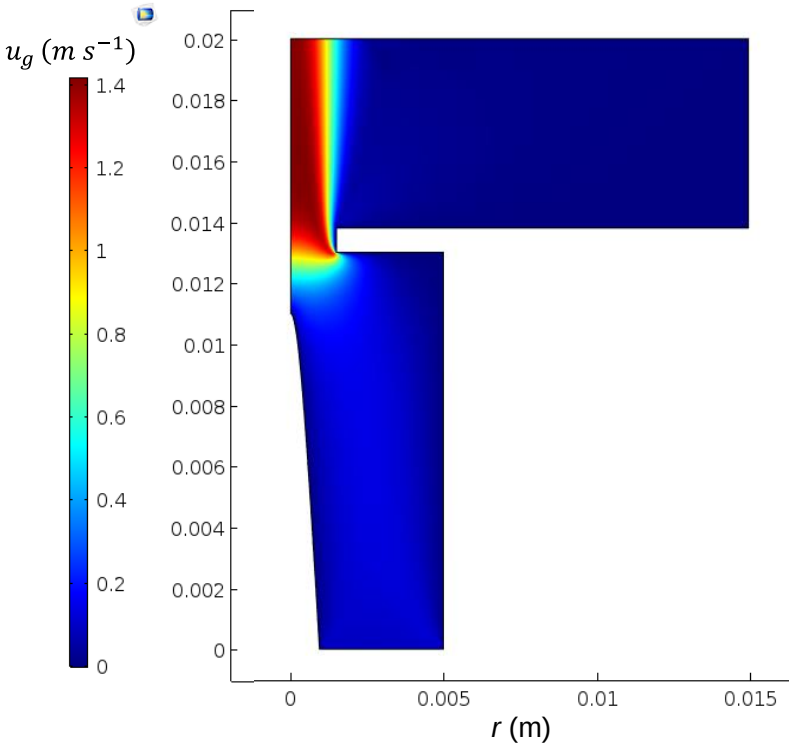

Fig. SI-4. Modulus of the gas velocity field (or gas speed). Air flows from the corona needle chamber to the electrospray domain. The gas velocity field has minimal impact on the behavior of the ions in the corona discharge chamber, due to the dominance of the electrical force.

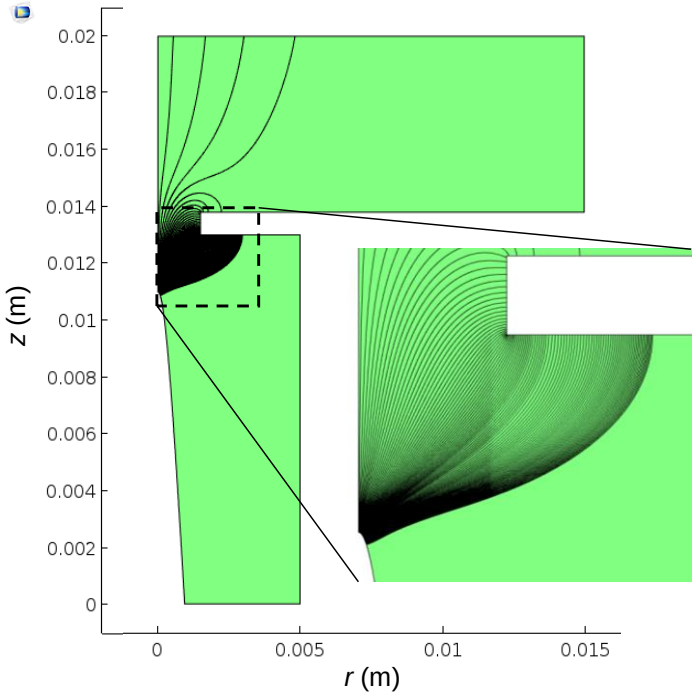

Fig. SI-5. Ion trajectories originating at the corona needle surface. The trajectories were computed considering that the velocity of the ions is given by $\mathbf{u_g} + K_{ion} \cdot \mathbf{E}$.

S2. Effect of the image droplets on the Taylor cone

In our procedure to compute the electric field in this article, the impact of the droplet images on the plate was accounted for according to Eq. (3). However, the droplet images on the Taylor cone and the capillary were neglected, for simplicity. To justify such omission we have conducted a comparative analysis of the electric field determined by either considering or ignoring the existence of induced charges on the cone due to the presence of nearby charges. Most of the induced charge is expected to be due to the nearest charges. Therefore, to simplify the analysis, we consider only the charges of the droplets which represent the jet charge in the article's spray simulations. For further simplicity, we assume that these droplets are not moving.

The first simulation method, referred to here as 'Full', involves solving the Laplace equation for computing the electric field for the system comprising a capillary, a Taylor cone, a counterplate, and 38 droplets evenly distributed between the tip of the Taylor cone and the jet breakup point for the acetone simulation. Note that this electric field solution inherently incorporates the contributions from the so-called image charges at the Taylor cone and the capillary (namely, the induced charges on the cone and on the capillary by the droplets' charges). The number of droplets coincides with the number of droplets in the jet for the acetone simulation.

Each droplet features a uniform charge surface density, ensuring that the total charge of a single droplet matches the average charge in the acetone simulation. The cone's voltage matches that of the acetone simulations, and the plate is Earth-grounded.

To avoid the singular solution of the Laplace equation at the cone's tip, the cone's apex has been replaced with a spherical cap possessing a radius equal to the average diameter of the droplets (8 μm). The distance between the cap's tip and the plate, has been set at exactly 2 cm.

This system has been numerically solved using COMSOL, giving special attention to achieving a solution that remains unaffected by variations in the size of the computational cell elements (defined in 3 regions of increasing mesh resolution towards the droplets and cone tip region).

Figures SI-6 to SI-8 show the results in terms of $\log_{10}(|E_z|)$ for various levels of magnification.

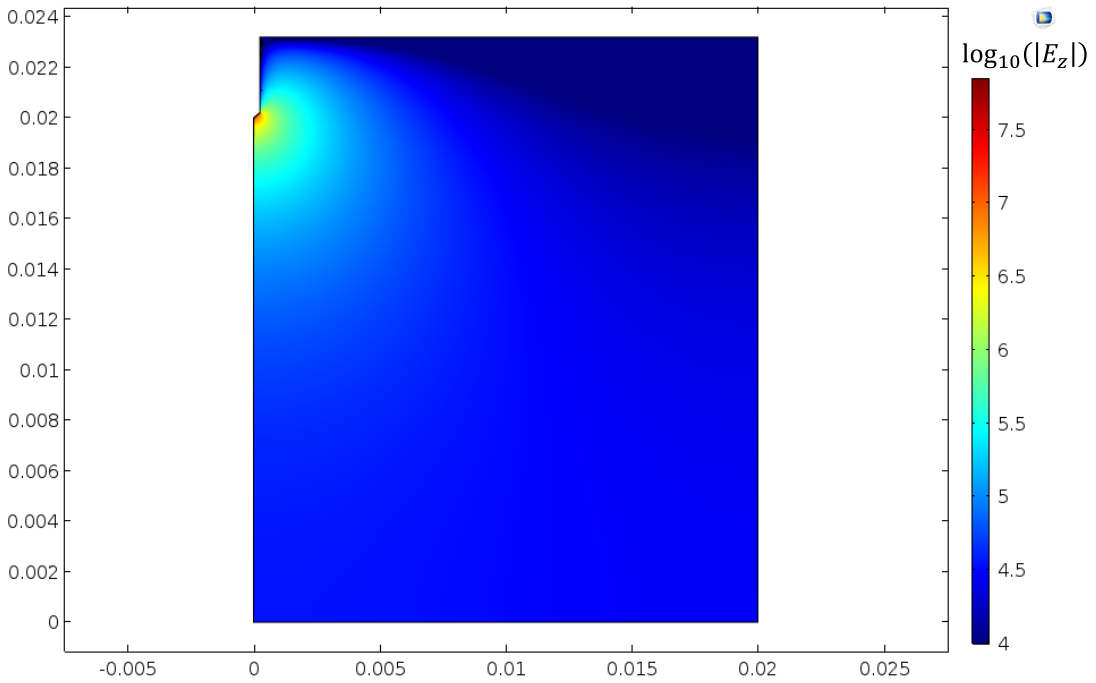

Fig. SI-6. General view of the Full system showing the base 10 logarithm of the absolute value of the z component of the electric field.

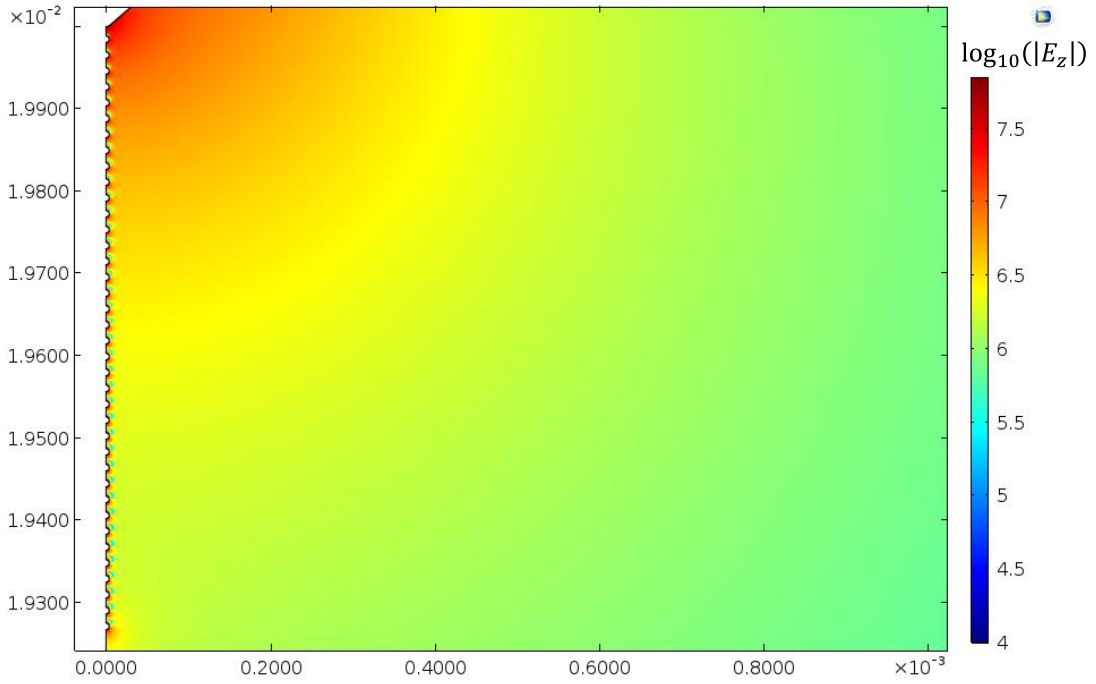

Fig. SI-7. A zoomed-in view of the results given in Fig SI-6, for a region near the end of the cone and the 38 droplets.

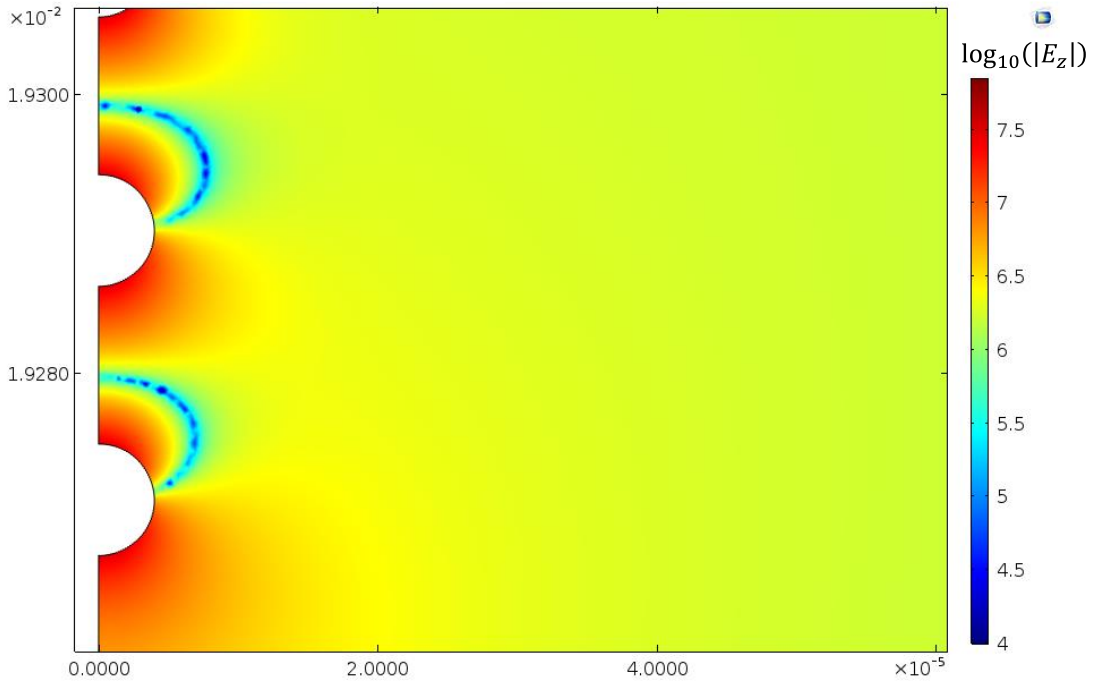

Fig. SI-8. A zoomed-in view of the results given in Fig SI-7, showing the $\log_{10}(|E_z|)$ around the two droplets located farthest from the cone tip.

The second simulation method, referred to here as 'Direct Droplet Contribution', has been conducted as it is done in the article (see equation (3)), namely, by ignoring the 'image charge' induced on the cone by the droplets. This is done by adding the external electric field due to the electrodes' potentials (and, in the paper, also due to the ions and the progenies generated in droplet's Coulomb fissions, which are ignored here), plus the electric field due to the droplets (and their image charges in the plate, ignored here) described using Coulomb's law. Mathematically, the complete electric field within the system is expressed as

$$\mathbf{E} = \mathbf{E_{CP}} + \frac{\bar{q}}{4\pi\varepsilon_0}\sum_{d=1}^{38}\frac{\mathbf{R}-\mathbf{R}_d}{(|\mathbf{R}-\mathbf{R}_d|)^3}$$

Here, $\mathbf{E_{CP}}$ is the component of the electric field stemming from the electrodes (here the capillary, the Taylor cone with rounded tip, and the plate), $\mathbf{R}$ represents the position vector at the point were the electric field is to be evaluated, $\mathbf{R}_d$ signifies the position vector of droplet d, and $\bar{q}$ denotes the average initial droplet charge (average charge of an acetone droplet upon emission).

The comparison of the electric fields obtained by the two methods provides an order of magnitude estimation for the error that is induced when excluding the image charges on the cone and capillary, as assumed in the text.

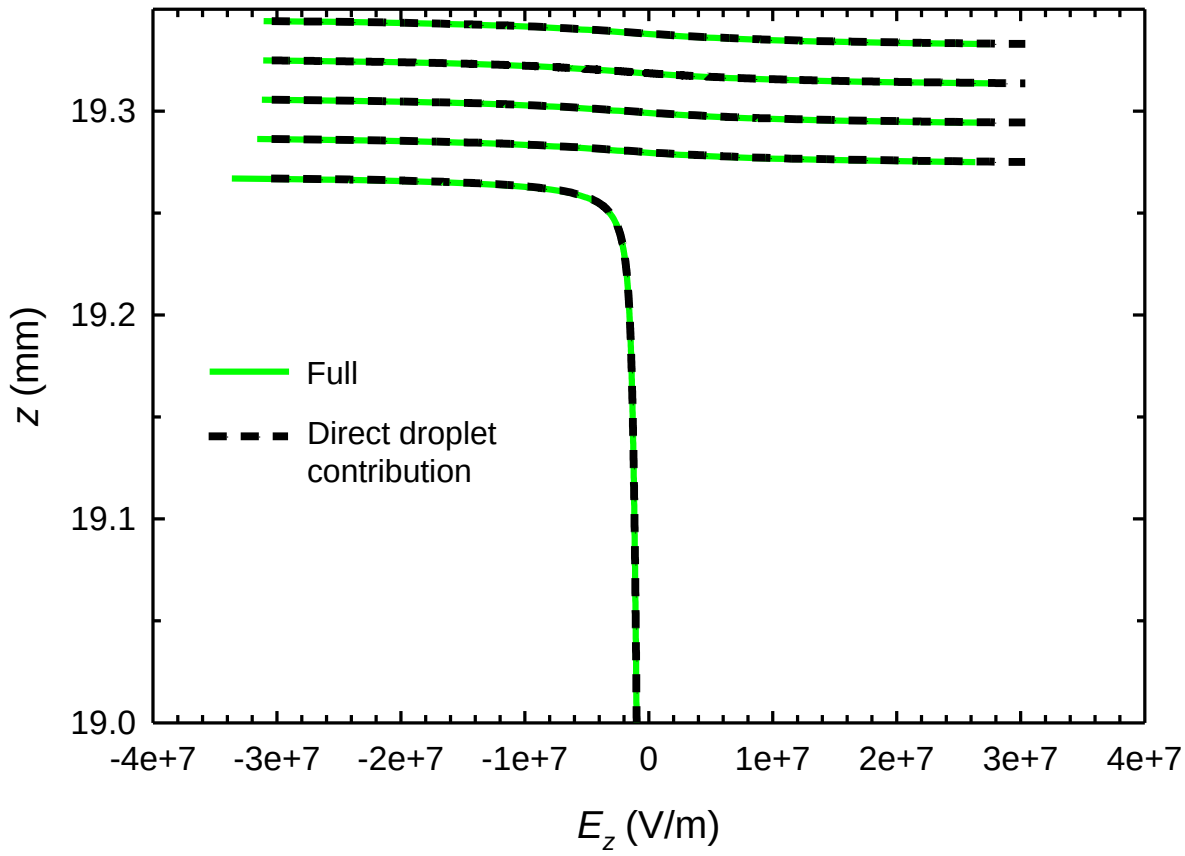

Fig SI-9. Comparison of the electric field along the z-axis obtained by the Full and Direct Droplet Contribution methods, within a range that includes the last five droplets and some region dowstream.

Figure SI-9 depicts the electric field distribution along the system axis within the range of $0.01935\ m \geq z \geq 0.01900\ m$. This interval encompasses both the last five droplets and some space beneath the last droplet. The figure shows that the two solutions closely resemble each other, with small differences. (Note that a negative electric field z component means that the field is pointing towards the plate, as the z coordinate increases in the "vertical" direction, from the plate.)

To assess the impact of disregarding image charges on the Taylor cone, and the capillary, Fig SI-10 illustrates the disparity between the outcomes resulting by both computation methods along the axis. The Figure includes both the absolute (Fig SI-10(a)) and the relative (Fig SI-10(b)) discrepancies. The upper part of the z-range of the graph includes the average position where the first "free" droplet is released in the article's simulations (a droplet that does not belong to the line of droplets that emulate the jet). At this specific location the relative discrepancy between both simulations is as low as 1.25 %, and decreases progressively in the downstream region into which the droplets will be moving. The effect is extremely small and

is expected to become progressively smaller as the distance between a travelling droplet and the Taylor cone increases. As for the case of charges near a planar surface (e.g., see Fig. 7 of Arumugham-Achari et al., 2013), most of the induced-charge effect on the Taylor cone and capillary comes from the charges nearest to the Taylor cone surface, with a rapidly decreasing contribution from the rest of the droplets. We therefore conclude that the image charges on the Taylor cone and capillary have a very small effect on the electric field, and can safely be omitted, as done in the article.

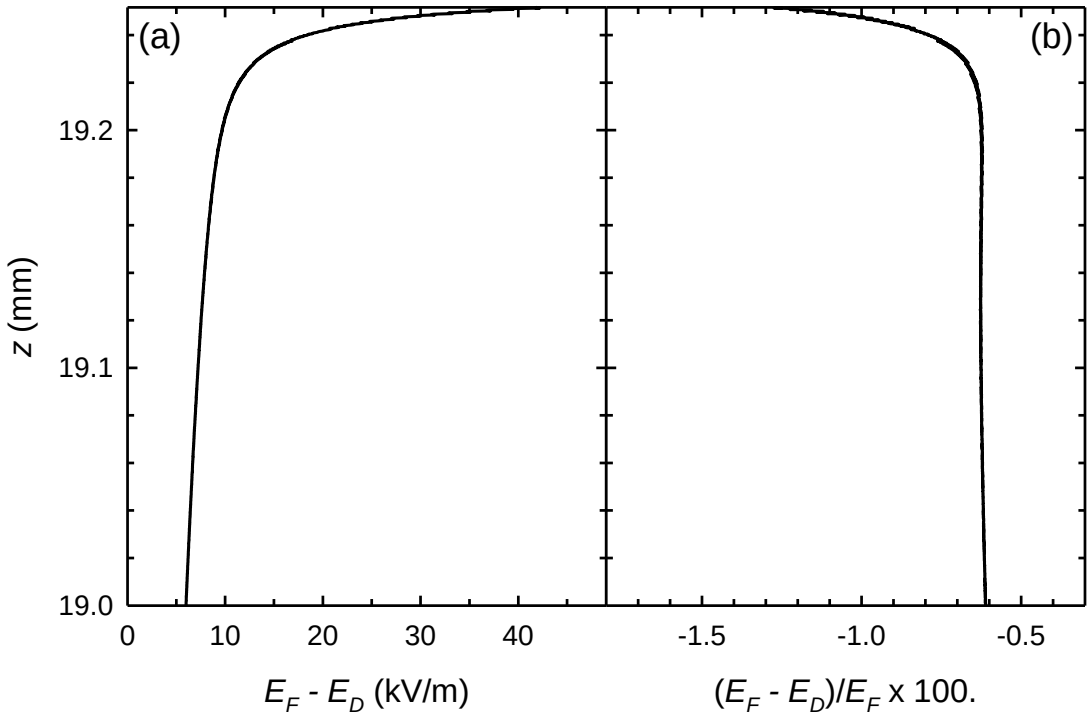

Fig. SI-10. (a) Difference between the electric fields computed with the 'Full' (F) and the 'Direct droplet contribution' (D) methods, from the average location of the first "free" droplet to 1 mm from the tip of the TC. (b) The same but in terms of percentage.

S3. Potentials and ion flux used as boundary conditions at the orifice and slit

In all the electrospray simulations with ions presented in the article, the electric potential and ion flux in the orifice are specified at the $z = H$ plane by functions obtained from the values of these variables in the corona discharge simulation described in section S1. These functions are shown in Figures SI-11 and SI-12, respectively.

In Figure SI-11, the plate potential is zero everywhere except at the orifice (through which the ions enter the electrospray domain) and at the slit (through which the droplets exit the electrospray domain). It is negative at the orifice due to the influence of the negative potential

of the corona needle and the ionic charge. The potential is positive at the slit, due to the influence of the positive electrodes (capillary and ring) and the concentric cylinders going down from the slit which are Earth-grounded. Figure SI-12 shows the flux of ionic charge. Near the wall the flux becomes negative, indicating the flyback of the outermost trajectories from the positive-flux part.

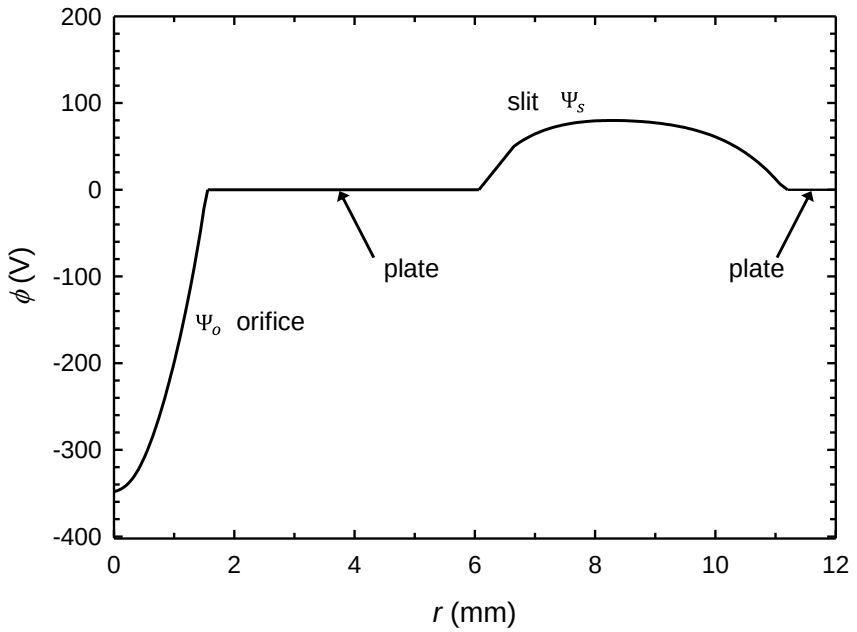

Fig. SI-11. Boundary conditions at the slit and orifice. Variation of the potential at the plane level close to the axis, showing the potentials of the orifice and slit that were used as boundary conditions.

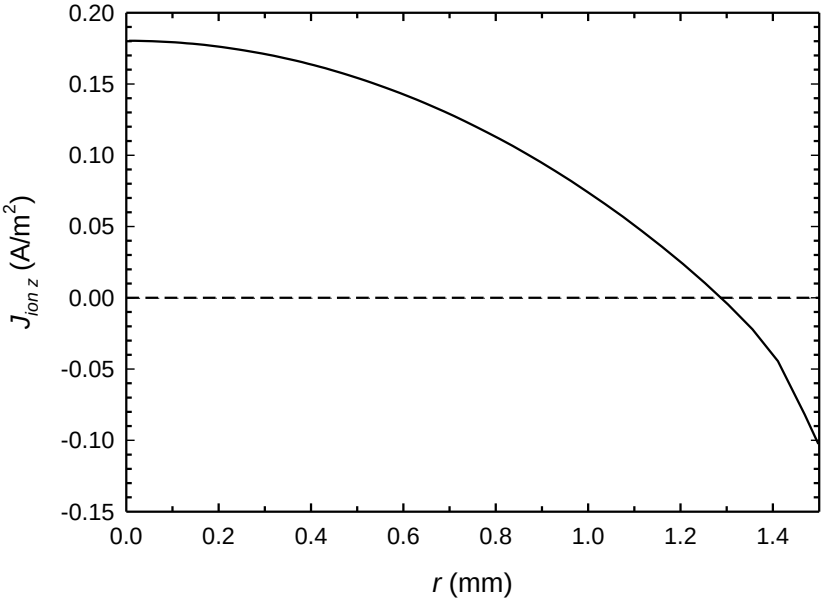

Fig. SI-12. Flux of charge taken from the corona discharge simulation used as boundary condition at the orifice.

S4. Droplet number evolution within the system

All the data represented in the Results section of this article are averages of variables in the pseudo-steady state condition. To determine the moment when the simulated system has attained such steady state, we monitor the number of droplets present within the system. Fig. SI-13 shows the time-evolution of this variable for one of the simulations. The simulations start by following the evolution of droplets *without* the presence of ions. In this part of the simulation, the droplets undergo Coulombic fission events; however, the progeny droplets are not accounted for in the figure. A pseudo-steady state, characterized by a nearly constant number of alive droplets, is quickly developed. At time 50 ms, after the system has reached pseudo-steady state in all the simulations, ions are admitted in the system. A new pseudo-steady state is obtained much later, after about 150 ms (0.2 ms since the start). The number of parent droplets becomes larger due to droplet accumulation in the computation domain, as the droplets are slowed down by the discharging process.

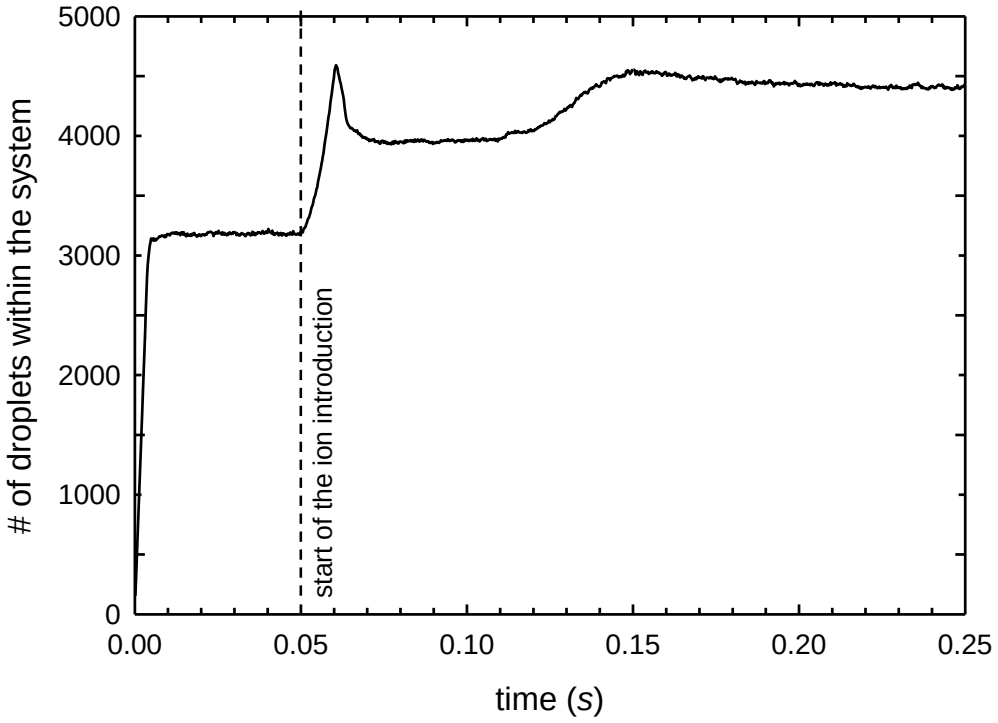

Fig. SI-13. Evolution of the number of main droplets (not counting the progeny droplets) within the system for the conditions of $\overline{u_{g0}}$ = 4 m/s and l_R = 2 mm. The electrospray simulation was initially conducted without ions for $0 \leq t \leq 0.05$ s during which period the number of droplets quickly stabilized to a pseudo-steady state. Ions were introduced into the system from t = 0.05 s resulting in fluctuations in droplet number until a new steady state was reached. When computing average values, only steady state periods were considered.

S5. Effect of the ring-over-capillary voltage ratio ($\eta \equiv \phi_R/\phi_C$) on the electric field

The capillary and ring voltages (ϕ_C and ϕ_R) with respect to the plate are computed by independently selecting their difference $(\phi_C - \phi_R)$ and their ratio $\eta \equiv \phi_R/\phi_C$. The voltage difference determines the stability of the Taylor cone, and is assumed to depend only on the liquid and the axial separation between the capillary and the ring l_{CR}, as described in section 4.1 of the article (also see the caption of Fig SI-14). The effects of the voltages ratio α on the electric field are described here.

Fig SI-14 shows, for constant voltage difference between the capillary and the ring, how the electric field around these electrodes changes as a function of η. As η increases between 0.4

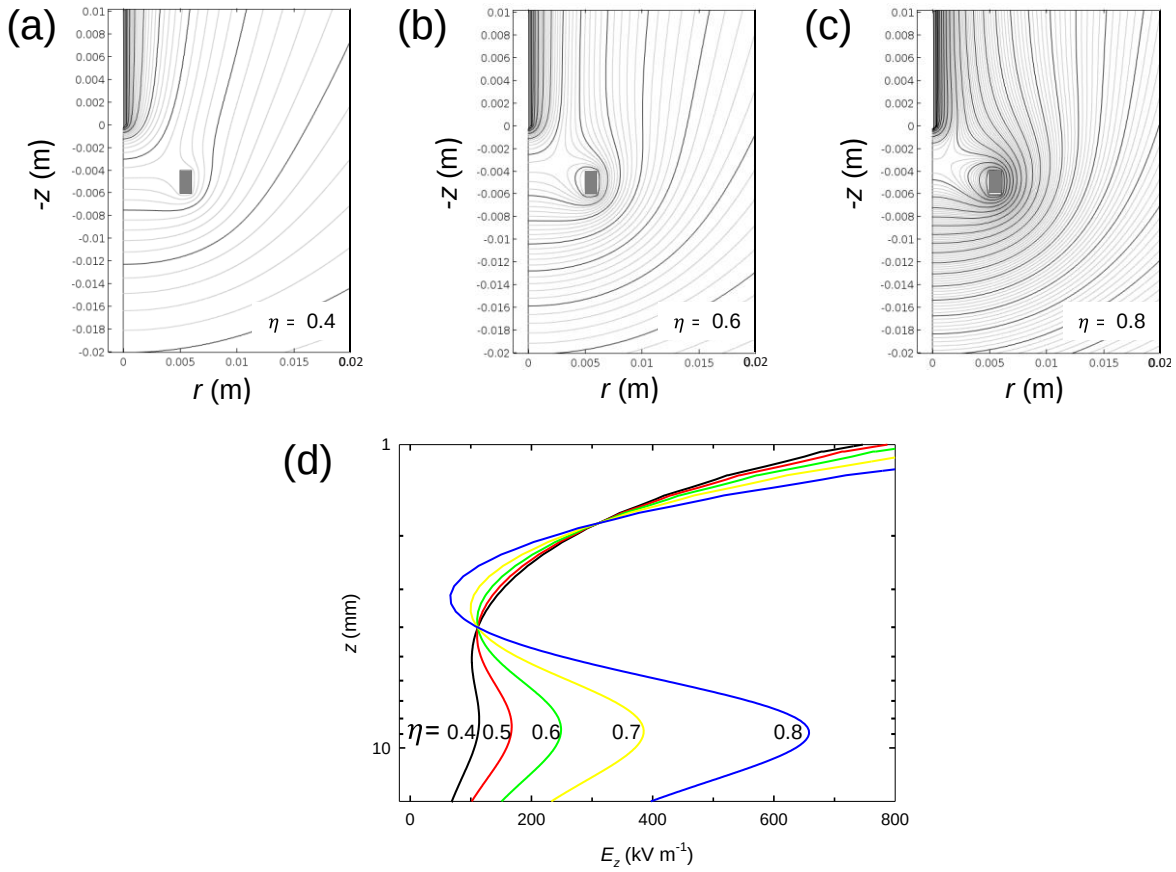

Fig. SI-14. Effect of the ring-to-capillary voltage ratio α on the electric field ($\eta \equiv \phi_R/\phi_C$), for the case of the acetone with $l_{CR} = 4$ mm and $l_R = 2$ mm. The onset electric potential difference between the capillary and the position $(r, z) = (0, 4)$ mm necessary to establish a Taylor cone was established as $\phi_C - \phi(0, 4) = 2806\ V$ (see the article's section 4.1). It is assumed that $\phi(0, 4) = \phi_R$. Panels (a-c) illustrate the equipotential lines for different η values of 0.4, 0.6 and 0.8, corresponding to $\phi_C = [\phi_C - \phi(0, 4)]/(1 - \eta)$ of 4677, 7015 and 14030 V. Panel (d) shows the z component of the electric field along the z-axis for different values of η.

and 0.6 (at $\phi_C - \phi_R$ of 2806 V), the field intensifies everywhere, with two important features: (1) the field's weakening in a region between the ring and the capillary, and (2) the stronger attraction of the field towards the lower inside wall of the ring. Both of these features are necessary to discourage the ions from reaching the Taylor cone.

For η of 0.8 (panel (c)), although the weak field region is maintained, the field becomes intense everywhere, with the equipotential lines becoming tighter also around the capillary and the Taylor cone. Indeed, as η approaches unity, the capillary and ring voltages will tend to diverge (become infinite) as well as the electric field at the Taylor cone. Therefore, eventually, as η becomes close enough to 1, the constancy of the capillary-to-ring voltage difference cannot ensure Taylor cone stability, causing operability difficulties and facilitating undesired electric discharges.

Finally, panel (d) shows the z component of the electric field along the z-axis for different values of η. This variable reaches a minimum about at the ring's position ($z = l_{CR} = 4$ mm).

Based on the forgoing facts, for the spray plumes simulations in this article we chose a value of η far from unity, chosen at 0.5 without further optimization.

S6. Effect of the ring height (l_R) and ring-to-capillary distance (l_{CR}) on the electrical field along the axis

We investigated the dependence of the electric field on the ring's height (l_R) and the ring-to-capillary distance (l_{CR}) without considering space charge (ions, droplets, progenies), by solving Laplace's equation for the electric potential $\nabla^2\phi = 0$.

Figure SI-15 shows the z component of the electric field along the axis (r = 0) within the range $0 \leq z \leq 0.015$ m for different heights of the ring l_R, for $l_{CR} = 4$ mm, η = 0.5, ϕ_C = 5612 V. This particular case illustrates the general trends which would be found for other similar values of these parameters. As l_R is increased the local minimum of E_z ($E_{z,min}$) decreases due to electrostatic shielding in the interior of the ring's hole, as expected. As l_R is reduced, the location of $E_{z,min}$ gets closer to the capillary, eventually ocurring above the upper end of the ring. Therefore, choosing a smaller l_R comes at the price of raising the value of the electric field, thus encouraging the passage of ions towards the Taylor cone.

Figure SI-16 shows the changes in E_z along the axis for various values of the capillary-to-ring distance l_{CR}, for a fixed ring height l_R = 2 mm. Raising l_{CR} causes the minimum of E_z to

decrease, while its location does not vary much. However, this comes at the price of raising the value of the capillary potential.

S7. Effect of ring height (l_R) on the spray plume without ions

In Fig. SI-17, we examine the strong effect of the ring height l_R on the spray's fate, for the case without corona ions. This figure shows the (r, z) droplet positions and electric equipotential lines for snapshots of sprays simulated under constant representative values of air volumetric rate (equal $\overline{u_{g0}}$) and electrodes' potentials.

Large zones of weak field strength can be easily identified in the figures' insets, by the increased spacing of the equipotential lines. As the ring becomes taller, the zone of weakened electric field grows in size. This is expected for constant electrodes' potentials, because, as the ring becomes taller, both the plate and the capillary become increasingly more shielded inside

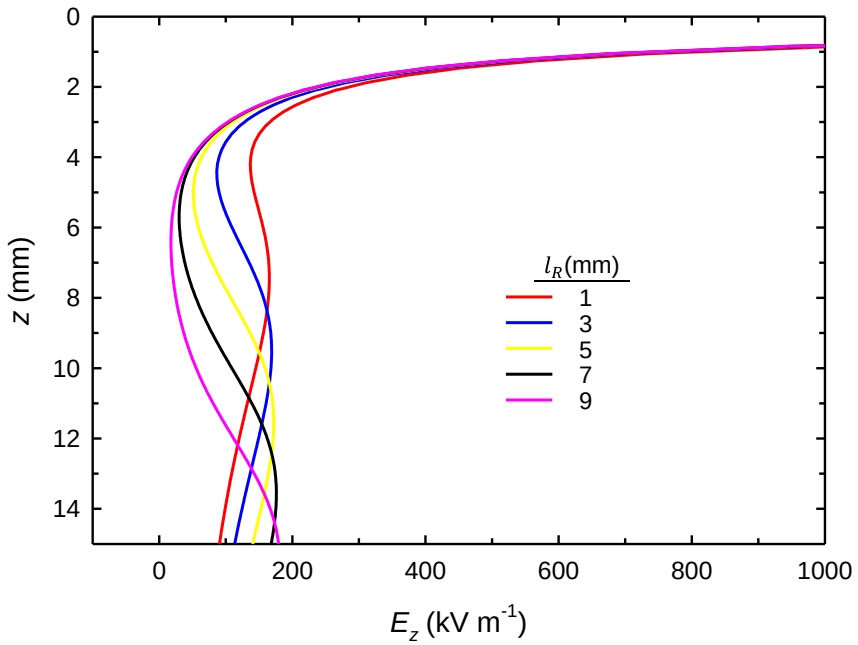

Fig. SI-15. z component of the electric field (abscissae) along the z axis (ordinate), for different ring heights (l_R) for the parameters l_{CR} = 4 mm, η = 0.5, ϕ_C = 5612 V.

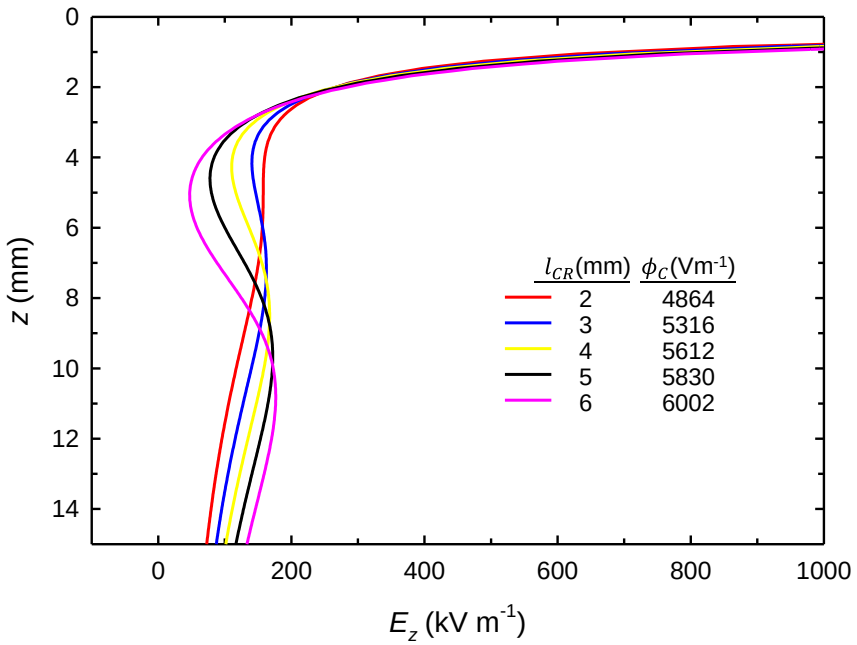

Fig. SI-16. z component of the electric field (abscissae) along the z axis (ordinate), for different ring-to-capillary separations (l_{CR}) shown in the figure, for l_R = 2 mm and η = 0.5. As explained in section 4.1, when l_{CR} changes so does ϕ_C.

the ring. In addition, the weakening of the field in the weak-field zone is remarkable at all ring heights: Because the electric field vector is a continuous function of position, it is easy to deduce that the field's modulus becomes zero at some point within the zone of highest spacing between equipotentials.

The spray behavior can be described as follows. Initially, up to $z \sim 3$ mm, all three sprays expand similarly, as the droplets' dynamics are governed by inertia and electrical forces mainly, and much less by air drag. Thereafter, as the ring becomes taller, the z component of the electric field becomes weaker near the axis, while the droplets become attracted more towards the larger ring. All this causes the spray to expand radially more, and to reach a critical condition at which trajectory reversal takes place for a set of droplet trajectories close to the spray periphery. This condition has been exceeded at the parameter values of panel (b) (l_R = 4 mm). The droplets with reversed paths are above the ring, and close to it, in a region where the electric field points upward and the airflow is decreasing its speed as the channel wall is approached (see Figure 4 in the main text). Droplets in more interior trajectories approach the ring in the weak-field zone, but do not reach it. Instead, the airflow pushes these droplets downward toward a zone below the symmetry plane of the ring where the electric field strength increases and the electric field vector points in a similar direction as the airflow. In this zone, the field points a bit inward, toward the axis, because of the ring and plate interaction.

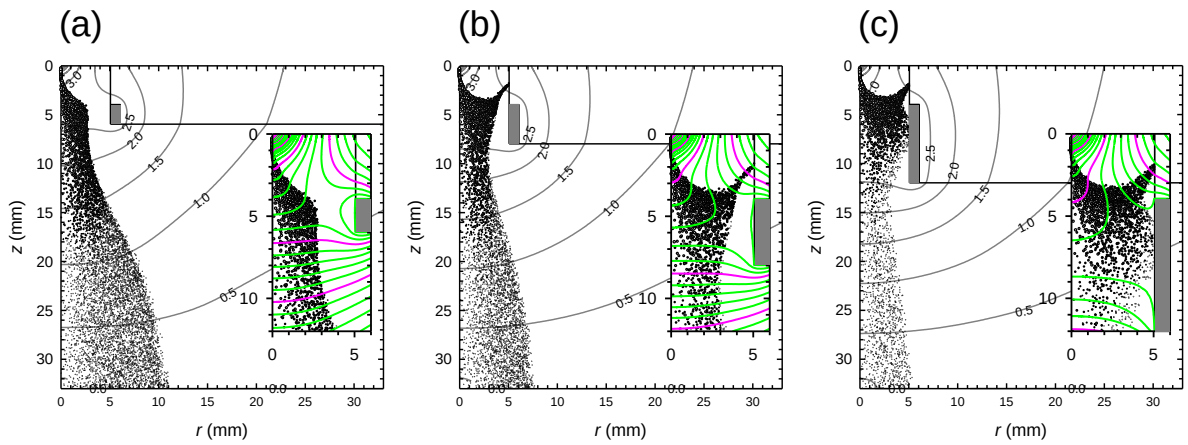

Fig. SI-17. Effect due to the height of the ring has on the spray behavior and the electric field. Snapshots and equipotential lines for electrosprays of acetone in the absence of corona ions, for $\overline{u_{0g}}$ = 1 m/s (average gas velocity at the upper gas inlet) and l_R = 2 mm (a), 4 mm (b) and 8 mm (c). The ring voltage is kept at 50% of the capillary voltage (ϕ_C = 5612 V = $2 \times \phi_R$). Panels (a) and (b), already shown in the article's main text, are repeated here to better see the trends. The insets show a zoomed-in of the upper spray region, where more detailed equipotential lines are shown. The purple lines are the same equipotential lines shown in the main panels (potential values shown in kV). The potential difference between consecutive lines in the inset is 100 V.

Eventually, for the tallest ring, shown in panel (c) (l_R = 8 mm), in addition to upstream flying trajectories, droplets from more inner trajectories end up depositing on the inner ring wall, as well. The droplet loss at the ring and dielectric is large, resulting in a much lower droplet population in the spray between the ring and the plate.

S8. Axial evolution of droplet charge ratio in absence of ions

Fig. SI-18 shows the z-dependence of the ratio of the droplet charge to its Rayleigh limit value. We plot the mean of that quantity (continuous black line) as well as plus and minus one standard deviation (red dotted lines). (Note, however, that the probability density function of the charge ratio cannot be symmetric, since values exceeding 1 are not allowed.) The graph shows, as expected, that the Rayleigh limit is approached and that, as soon as Coulomb fission (CF) events take place, the mean stops increasing. However, the mean stops growing below unity. This is not surprising because the droplets found at a given z have undergone different histories, and therefore hold charges that are at different ratios from their Rayleigh limit.

After reaching a maximum value, the charge-ratio mean decreases with z, as the droplet histories diversify at different radial positions and the standard deviation increases. For a while (~$0.15 < z <$ 0.023 m), however, the mean plus one standard deviation remains nearly constant. Thereafter ($z >$ 0.023 m), all three traces decrease while undergoing a couple of ripples. These ripples reflect the fact that the intensity of CF events is intensified in some regions.

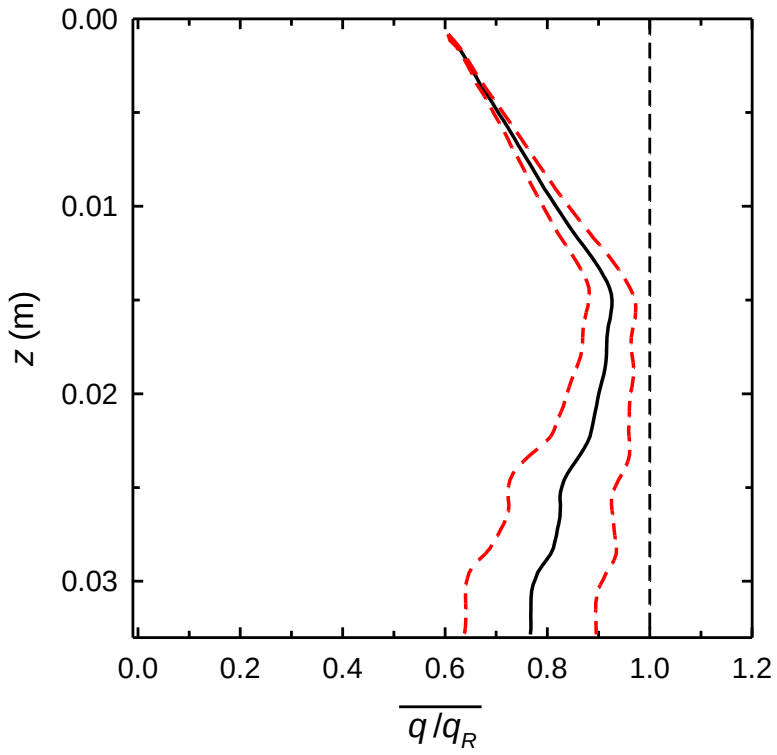

Fig. SI-18. Axial evolution of the ratio of droplet charge to its own Rayleigh limit charge. The black continuous line shows the average value (taken at a given z), while the red-dotted lines represent the average plus and minus one standard deviation. The system is identical to the one shown in Fig. 6(c) in the main text; that is, an electrospray of acetone without ions, with l_R = 2 mm and $\overline{u_{0g}}$ = 4 m s^{-1}.

S9. Current due to ions and droplets for acetone for various gas flows

Figure SI-19 shows the z-profiles of the currents associated with the ions, the spray and their sum (total current) for three values of the upper inlet gas speed $\overline{u_{g0}}$ (1, 2 and 4 m/s). These graphs extends the similar figure from the article, Figure 9, which corresponds to 4 m/s and is repeated here for better display of the trend. The droplet discharging is initiated similarly in all cases. However, upon increasing the gas speeds, the spray discharging zone extends towards

the plate, as the droplets travel faster under the balance of the electric and drag forces (which are nearly balanced as the droplet inertia is much smaller than either force). The ion concentration and electric field between these three cases is similar. Therefore, the convective time needed to reach a certain droplet charge is achieved further downstream when the droplet travels faster, due to the discharge kinetics.

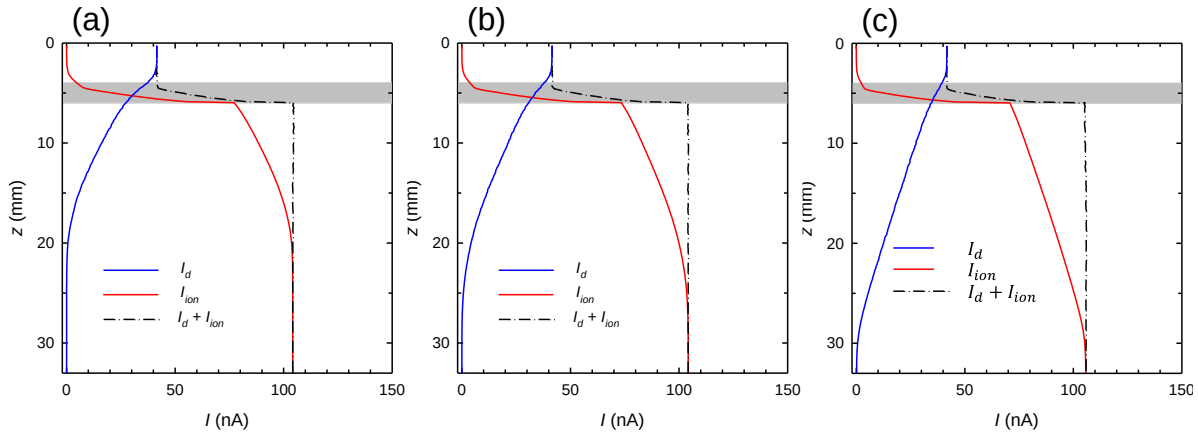

Fig. SI-19. Electric currents for acetone droplets (I_d) and ions (I_{ion}), with a ring height of 2 mm and two upper inlet gas speeds of 1 m/s (a), 2 m/s (b), and 4 m/s (c).

S10. Effect of ions and droplets on the air velocity field

Our study does not consider the influence of the ions' and droplets' motions on the air velocity field. In this section, we provide justification for this omission.

It is well-established that the movement of droplets and ions can alter the air velocity field (Arumugham-Achari et al., 2013; Qu et al., 2021). However, these alterations have primarily been observed in external flow systems, where the air velocity field is not confined by walls. In our case (internal flow), the presence of walls limits the degree to which the ions' and droplets' motions can influence the air velocity field. In our system, the volumetric flow rates are given at both the inlet and outlet as boundary conditions, which impose the average air speed through any given cross-sectional area. Therefore, while neglecting the effects of ions and droplets may lead to local variations in the air velocity profiles it cannot change the average speed. In other words, the forces exerted by ions and droplets on the air do not translate into global velocity changes, but rather, into changes in the pressure gradients that maintain these flows.

Furthermore, studies investigating ion winds generated by corona discharges (Goldman et al., 1985; Béquin et al, 2003, Guan et al., 2018) have primarily been conducted in systems where the current levels are on the order of microamperes. In our study, the corona discharge generates 14.3 microamperes, but the current entering the electrospray chamber is only approximately 0.1 microamperes. Such current reduction arises because the walls surrounding the corona discharge needle collect most of the generated ions, while only a tiny fraction passes through the orifice. This substantial reduction in current entering the electrospray chamber significantly reduces the potential impact that the ions may have on the air velocity.

To further substantiate this argument, we report the rate at which the ions transmit mechanical energy to the air, denoted as $\dot{E}_{ion}$. It has been computed for an example simulation (specifically, the one involving acetone with $\overline{u_{g0}}$ = 4 m/s and l_R = 2 mm). This computation has involved integrating the dot product between the electric force acting on the ions and the air velocity vector, across the entire volume of the electrospray chamber:

$$\dot{E}_{ion} = \int_V \rho_{ion}\, \mathbf{E} \cdot \mathbf{u}_g \, dV$$

The computed $\dot{E}_{ion}$ value is 2.80 × 10^{-5} W. This value can be put in context by comparing it to the rate at which kinetic energy enters the system at the upper gas inlet, computed for the entering area (S) between the capillary and the dielectric as

$$\dot{E}_c = \frac{1}{2}\rho \int_S {u_g}_z^3 \, dS$$

This integral is $\dot{E}_c$ = 5.20 × 10^{-3} W. Clearly, $\dot{E}_c \gg \dot{E}_{ion}$, reinforcing our argument that the impact of the ionic wind on the pressure and air velocity fields should be minimal in our simulations.

References

Adamiak, K., & Atten, P. (2004). Simulation of corona discharge in point-plane configuration. *Journal of Electrostatics*, 61(2), 85–98. https://doi.org/10.1016/j.elstat.2004.01.021

Adamiak, K., Atrazhev, V., & Atten, P. (2005). Corona discharge in the hyperbolic point-plane configuration: Direct ionization criterion versus approximate formulations. *IEEE*

Transactions on Dielectrics and Electrical Insulation, 12(5), 1025–1033. https://doi.org/10.1109/TDEI.2005.1522195

Arumugham-Achari, A. K., Grifoll, J., & Rosell-Llompart, J. (2013). Two-way coupled numerical simulation of electrospray with induced gas flow. *Journal of Aerosol Science*, *65*, 121–133. https://doi.org/10.1016/j.jaerosci.2013.07.005

Béquin, P., Castor, K., & Scholten, J. (2003). Electric wind characterisation in negative point-to-plane corona discharges in air. *Eur. Phys. J. AP*, 22(1), 41–49. https://doi.org/10.1051/epjap:2003006

Goldman, M., Goldman, A., & Sigmond, R. S. (1985). The corona discharge, its properties and specific uses. *Pure and Applied Chemistry*, *57*(9), 1353–1362. https://doi.org/10.1351/pac198557091353

Guan, Y., Vaddi, R. S., Aliseda, A., & Novosselov, I. (2018). Experimental and numerical investigation of electrohydrodynamic flow in a point-to-ring corona discharge. *Physical Review Fluids*, *3*(4), 1–14. https://doi.org/10.1103/PhysRevFluids.3.043701